Available online at www.sciencedirect.com

ScienceDirect

Geochimica et Cosmochimica Acta 247 (2019) 1–26

Geochimica et Cosmochimica Acta

www.elsevier.com/locate/gca

Quantifying weathering rind formation rates using *in situ* measurements of U-series isotopes with laser ablation and inductively coupled plasma-mass spectrometry

Lin Ma[a,*], Anthony Dosseto[b], Jerome Gaillardet[c], Peter B. Sak[d,e], Susan Brantley[e]

[a] *Department of Geological Sciences, University of Texas at El Paso, El Paso, TX 79968, USA*
[b] *Wollongong Isotope Geochronology Laboratory, School of Earth and Environmental Sciences, University of Wollongong, NSW 2522, Australia*
[c] *Institut de Physique du Globe de Paris, France*
[d] *Department of Earth Sciences, Dickinson College, Carlisle, PA 17013, USA*
[e] *Earth and Environmental Systems Institute, Pennsylvania State University, State College, PA 16802, USA*

Received 27 May 2018; accepted in revised form 13 December 2018; Available online 21 December 2018

Abstract

To quantify chemical weathering processes, it is essential to develop and utilize new geochemical tools that can provide information about chemical weathering in the field. U-series isotopes have emerged as a useful chronometer to directly constrain the rates and duration of chemical weathering. However, the conventional solution-based MC-ICPMS method involves a long and expensive sample processing procedure that restricts the numbers of measurements of samples by U-series analysis that can be completed. Here, we report *in situ* measurements of U-series disequilibria obtained with laser ablation (LA)-MC-ICPMS on weathering rinds collected from the tropical island of Basse-Terre in the archipelago of French Guadeloupe. We characterized two weathering rinds for U-series isotope compositions and elemental distributions with LA-MC-ICPMS and LA-Q-ICPMS. The *in situ* measurements of U-series disequilibria were consistent with the previous bulk measurements obtained by conventional solution MC-ICPMS despite the larger analytical uncertainties. The LA technique allowed a greater number of measurements that accelerated sample throughput and improved spatial resolution of measurement. The rind formation age, weathering rates, and U-series mobility parameters modeled in this study are comparable to the results from previous studies conducted on the same clasts, and also reveal new insights on rind formation such as the impact of micro-fractures on weathering history and U-series ratios. The improved spatial resolution available with LA Q-ICPMS helps distinguish between linear and power law rind thickness-age relationships that were unresolvable using conventional solution-based MC-ICPMS. *In situ* measurements with LA-Q-ICPMS in these weathering rinds also elucidates the sequences of mineral reactions during chemical weathering. The LA-Q-ICPMS maps of major and trace elements and elemental ratios reveal details about the rind formation processes at the weathering interfaces of clasts such as dissolution of primary phases, formation of new phases, development of porosity, and mobility behavior of U. This study demonstrates a new analytical method for determining weathering rates in rinds rapidly and accurately that can be used in a large number of rinds, providing key information at the clast scale.

---

[*] Corresponding author.
E-mail address: lma@utep.edu (L. Ma).

https://doi.org/10.1016/j.gca.2018.12.020

1. INTRODUCTION

Chemical weathering plays critical roles at Earth's surface such as regulating the global carbon cycle (Walker et al., 1981; Berner et al., 1983; Drever, 2004), controlling water chemistry for hydrosphere (Gaillardet et al., 1999), supplying mineral nutrients to terrestrial ecosystems (Chadwick et al., 1999; Derry et al., 2005), and producing erodible materials for landscape evolution (Pavich, 1986; Anderson et al., 2002; Hilley and Porder, 2008). Despite the fundamental importance, we still lack effective tools to measure the weathering rates, especially in field studies, in order to fully understand how they respond to changes in landscape positions, climate, and tectonic regime. Many measurements of field-derived rates require that the duration or the age of the chemical weathering system is known. In many cases such independent age control is not available. It is essential to develop and utilize new geochemical tools that can directly measure chemical weathering rates.

U-series isotopes in weathering products have shown potential for quantifying the rates and duration of chemical weathering and erosion (e.g., Sarin et al., 1990; Dequincey et al., 2002; Maher et al., 2004; Krishnaswawi et al., 2004; DePaolo et al., 2006; Dosseto et al., 2008a,b; Pelt et al., 2008; Bourdon et al., 2009; Ma et al., 2010, 2012; Suresh et al., 2013; also reviews by Chabaux et al., 2003, 2008; Dosseto, 2015). Such an approach relies on U-series isotope disequilibria that result from fractionation of radionuclides of U, Th, and Ra due to different decay half-lives and geochemical properties (e.g., Ivanovich and Harmon, 1992; Bourdon et al., 2003). These radionuclides have long been used as a geochronologic tool with a closed system assumption to date processes such as magmatic differentiation or carbonate deposition (e.g., reviews by Condomines et al., 2003; Edwards et al., 2003). Mobility behaviors of U-series isotopes (e.g., ^{238}U, ^{234}U, ^{230}Th, and ^{232}Th) during low temperature water-rock interactions have been studied in detail, especially under open system conditions at weathering interfaces in clasts, soil profiles or watersheds where chemical weathering processes occur (e.g., reviews by Chabaux et al., 2003, 2008). This has enabled U-series isotopes to emerge as a useful chronometer to directly constrain the rates and duration of chemical weathering with timescales $<\sim$1.25 Ma (e.g., Vigier et al., 2001; Dosseto et al., 2008a; Pelt et al., 2008; Ma et al., 2010, 2012; Engel et al., 2016). In those studies, U-series isotope compositions in weathering rinds, soils, and river sediments have been typically measured using a solution-based method with multi-collector inductively coupled plasma mass spectrometers (MC-ICPMS). This method involves a time-consuming procedure that includes sample preparation (bulk or micro-drilled for $\sim$100 mg solid samples), sample dissolution and spiking, column separation and purification of U-series isotopes before measurements on MC-ICPMS (e.g., review by Chabaux et al., 2003). The solution-based MC-ICPMS method produces U-series isotope measurements with high precision and accuracy, with typical uncertainties of isotope ratios <0.5%. However, the long and expensive sample processing procedure is considered as a critical time-limiting step for providing fast sample throughput and generating large numbers of measurements of U-series analysis, especially for those chemical weathering studies in where a large number of analyses or high sampling spatial resolution are essential to examine weathering systems with different spatial or temporal scales.

The coupling of laser ablation (LA) with ICPMS technique has facilitated *in situ* measurements of detailed elemental profiles or maps on various geological and environmental materials for more than 30 years (e.g., Sylvester and Jackson, 2016). Recent developments in both instrumentation and methodology have allowed for high precision isotope ratio determinations such as U-series disequilibria by combining LA with MC-ICPMS for earth, environmental and archeological sciences (Sylvester and Jackson, 2016). These advances now provide the ability to extract various age and isotopic tracer information at μm-scale resolutions. For example, *in situ* U-series measurements (^{234}U/^{238}U and ^{230}Th/^{238}U) can be obtained at spots with a spatial resolution of <100 μm in carbonate samples that contain ppm-level of U concentrations (Eggins et al., 2005; Potter et al., 2005; McGregor et al., 2011; Spooner et al., 2016). Despite that the LA-MC-ICPMS method does not provide the highest precision and accuracy of U-series isotope measurements (typical uncertainties of LA-MC-ICPMS measurements are percentage level), LA offers several unique advantages over the conventional solution-based MC-ICPMS method including: (1) increased spatial resolution of the distribution of U-series isotopes at scales <100 μm; (2) minimal sample preparation time (no sample digestion or column chemistry needed); (3) rapid isotope measurements that allow for high sample throughput and large number of data points during analysis; and (4) non-destructive (or minimal destruction) sample analysis (e.g., Eggins et al., 2005; Potter et al., 2005; McGregor et al., 2011; Spooner et al., 2016). Here, we report *in situ* measurements of U-series disequilibria with LA-MC-ICPMS on two weathering rind samples collected from the tropical island of Basse-Terre Island in French Guadeloupe (Fig. 1). This study is among the first studies that aim to directly date chemical weathering processes using *in situ* measurements of U-series disequilibria in silicate weathering products (e.g., Bernal et al., 2006). Unlike Bernal et al. (2006) who dated supergene Fe-oxy/hydroxides under an assumption of a closed system of U-series dating, here we investigated two weathering rinds developed from andesitic parent materials under open system behavior of U-series isotopes during chemical weathering. Weathering rinds are permeable and altered weathering products that envelop an unweathered parent core (collectively known as weathering clasts) and are commonly found in soil profiles developed under various types of climate and lithology (e.g., Sak et al., 2004, 2010). Weathering rinds provide a valuable medium to study the initiation and duration of chemical weathering in field systems, due to the presence of an easily identified core-rind boundary and the apparent absence of physical erosion during rind formation (e.g., Sak et al., 2010; Pelt et al., 2008; Ma et al., 2012). In this study, we demonstrated that the LA-MC-ICPMS technique can directly measure the duration and rates of weathering rind formation. Our study highlights the potential for using

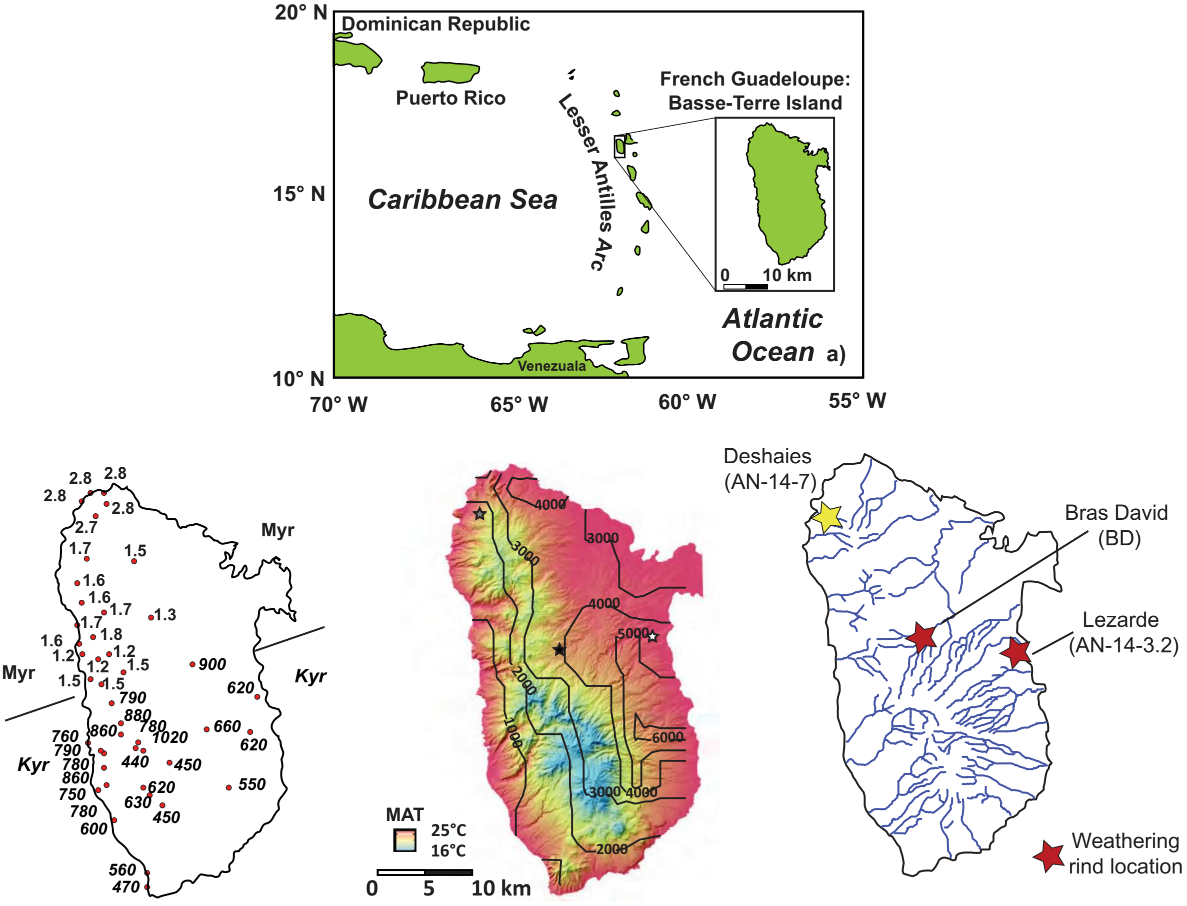

b) Bedrock ages c) MAP and MAT d) Rivers and watersheds

Fig. 1. (a) Basse-Terre Island in French Guadeloupe and the Caribbean region; (b) Bedrock ages from Ar-Ar dated lavas on Basse-Terre Island (Samper et al., 2007); (c) Orographic patterns of mean annual precipitation (MAP: mm yr^{-1}, TRMM data source) and mean annual temperature (°C); (d) Rivers and watersheds: sample locations of Bras David (BD; Ma et al., 2012), Lezarde (AN-14-3.2; Sak et al., 2018), and Deshaies (AN-14-7; Engel et al., 2016) are indicated.

in situ measurements of U-series disequilibria by LA-MC-ICPMS to quantify weathering rates, with considerable analytical advantages compared to the solution-based MC-ICPMS method. We also used laser ablation coupled to a single-collector quadrupole ICPMS (LA-Q-ICPMS) to map trace element distributions such as U concentrations, and to characterize rind formation processes including dissolution, formation of new phases, development of porosity, and mobility behavior of U at the weathering interface (core-rind boundary) of clasts.

2. MATERIALS AND METHODS

2.1. Geology and climate of Basse-Terre Island

Basse-Terre Island, a part of the French Guadeloupe archipelago, is located in the Lesser Antilles volcanic arc (Fig. 1a; e.g. Jordan, 1975; Hawkesworth and Powell, 1980). Basse-Terre has been utilized as an important field site for exploring the impacts of precipitation on chemical weathering rates, both on short and long time scales, because of steep gradients in bedrock age, relief, and precipitation (Fig. 1; as a Critical Zone Observatory managed by IPGP and OSCAR; https://morpho.ipgp.fr/Obsera). The relatively homogenous bedrock composition makes Basse-Terre an ideal location to study chemical weathering under different climatic conditions with different aged bedrock while holding parent material composition constant. Volcanic materials form bedrock, lava flows, lava domes, pyroclastic deposits, and volcanic-clastic debris flows, with volcanic eruption ages between 2.8 Ma and 8.5 ka to present (Fig. 1b), and all are with similar andesite to basaltic-andesite compositions across the island (Samper et al., 2007).

Topographic variability on the island closely mimics the bedrock age, with high relief and steep slopes in the young southern areas and lower relief and gentler slopes in the much older and more stable northern part. Basse-Terre Island is characterized by a steep gradient in precipitation. Because of the north-south trending topographic divide on the island and the prevailing Atlantic winds from the east, the average annual precipitation (MAP) on Basse-Terre

Island is largely controlled by a pronounced orographic effect, ranging from <2000 mm to >6000 mm (Fig. 1c). Notably, the east and south coasts receive higher MAP and the leeward west and north coasts generally receive lower MAP. At the same time, the island experiences a near constant mean annual temperature of 25 °C, at sea level.

2.2. Clast site descriptions

Two weathering clast samples previously collected from Brad David (Sak et al., 2010; Ma et al., 2012) and Lezarde (Sak et al., 2018) watersheds of the Basse-Terre Island (Fig. 1d) were selected for *in situ* U-series measurements in this study. Site descriptions (see Table 1) and details of sample collection are summarized below for reference.

The Bras David clast (BD) (Fig. 2A–C) was collected from a thick regolith profile within the Bras David watershed from the central part of Basse-Terre Island (Fig. 1). The rugged Brad David watershed is in a humid, tropical environment with a mean annual temperature of ~23 °C (at average elevation ~300 m) and an annual precipitation about 3500 mm (Lloret et al., 2011; Tropical Rainfall Measuring Mission data; pmm.nasa.gov). The watershed is underlain by late Quaternary volcaniclastic debris flow deposits of dominantly andesitic to basaltic compositions (Samper et al., 2007). Volcanic flows in the region where the clast was collected were emplaced 900 ka before present, based on Ar/Ar dating (Samper et al., 2007).

In the Brad David watershed, thick weathering profiles (>10 m) develop in the volcanic debris flow deposits. The regolith is partially to completely depleted with respect to most primary minerals including pyroxene and plagioclase as well as the glass matrix, and is enriched in Fe oxyhydroxides, gibbsite and kaolinite (Buss et al., 2010; Clergue et al., 2015). The regolith is capped by a thin veneer of soil. In the regolith that is exposed at road cuts and excavations, rock fragments at various stages of weathering are commonly observed (Fig. 2A). Here, we refer the weathering rock fragments as weathering clasts. The formation of weathering clasts in regolith profiles is related to processes such as the mechanical fracturing of bedrock that produce rock fragments, which migrate upward through the regolith from the perspective of a land surface experiencing physical denudation. Other processes such as pyroclastic flows may also introduce rock fragments into regolith profiles to form weathering clasts. The clast (Fig. 2B) was from the B-horizon of a soil profile at 0.8 m depth in the Bras David watershed. In the field, weathered clasts are readily distinguished from the matrix by textural and color variations (Fig. 2B; Sak et al., 2010). The weathering rind material is brownish yellow (Fig. 2B), and the surrounding soil matrix material is a dark yellowish red (Fig. 2A).

The second clast sample (AN-14-3.2) was collected from a deposit exposed to a similarly warm and wet climate in the Lezarde watershed (Fig. 2D, E, –F–). The Lezarde watershed is located on the east part of the Basse-Terre Island, with a mean annual temperature of ~25 °C (at average elevation ~20 m) and an annual precipitation about 4500 mm (Tropical Rainfall Measuring Mission data; pmm.nasa.gov) (Fig. 1). The parent bedrock in the watershed is composed of volcaniclastic debris flow deposits of dominantly andesitic to basaltic composition, with an Ar/Ar dating age of ~600 ka (Samper et al., 2007). The sampled road cut in the Lezarde watershed exposes a well-developed (2–15 m thick) weathering profile formed on volcaniclastic debris flows (Fig. 2D). Within the steep faced exposure of the sampled road cut, two debris flows were distinguished in the field by color, texture, and abundance of weathered rock fragments (Sak et al., 2018). The clast sample (Fig. 2D) was collected from the B-horizon of the lower debris flow.

2.3. Sample collection and preparation

During sample collection in the field, before the clast was removed from the exposure, the orientation of the vertical axis was marked on the clast. Then the clast was carefully removed from the outcrop, preserving the friable rind and matrix material overlying the unweathered core, and immediately wrapped in aluminum foil and masking tape in the field to preserve the structure of the overlying rind and matrix material. Orientation information was then marked on the exterior of the wrapped clast. As the sampled clast was extracted from the exposure, some rind material from the underside of the clast detached and remained in the exposure (e.g., for sample BD).

In the laboratory, the clast was immersed in molten wax before complete unwrapping to preserve rind structure. The clast was removed from the wax bath and allowed to cool for 24 h, before the excess wax on the exterior was removed by heating to 55 °C for 8 h in a laboratory oven. The wax-impregnated clast was separated into two sections by cutting a vertical section along the major axis (Fig. 2B for BD; E for AN-14-3.2). Thin section billets (Fig. 2C and F) were cut from one half of the clasts and samples for chemical and isotopic analyses were collected from the other half (Fig. 2B and E). Pelt et al. (2008) analyzed the same type of wax used in the field after digestion by ICP-OES and ICP-MS and major and trace element contents of the wax are insignificant and did not contribute the blanks of the following analyses.

2.4. Solution-based MC-ICPMS for U-series isotope measurements

Rind and core samples for bulk U-series isotopic analyses were obtained by drilling powder material using a 3.175 mm diameter carbide-tipped bit (Fig. 2B and E). U and Th concentrations and isotopic ratios in drilled samples for Brad David rind sample (BD) and Lezarde rind sample (AN-14-3.2) were determined at the University of Texas at El Paso and were reported in Ma et al. (2012) and Sak et al. (2018), respectively. The previous results are summarized in Table 2.

2.5. *In situ* LA MC-ICPMS for U-series isotope measurements

In situ U and Th isotope analysis was performed by laser ablation multi-collector ICPMS (LA MC-ICPMS) at the Wollongong Isotope Geochronology Laboratory,

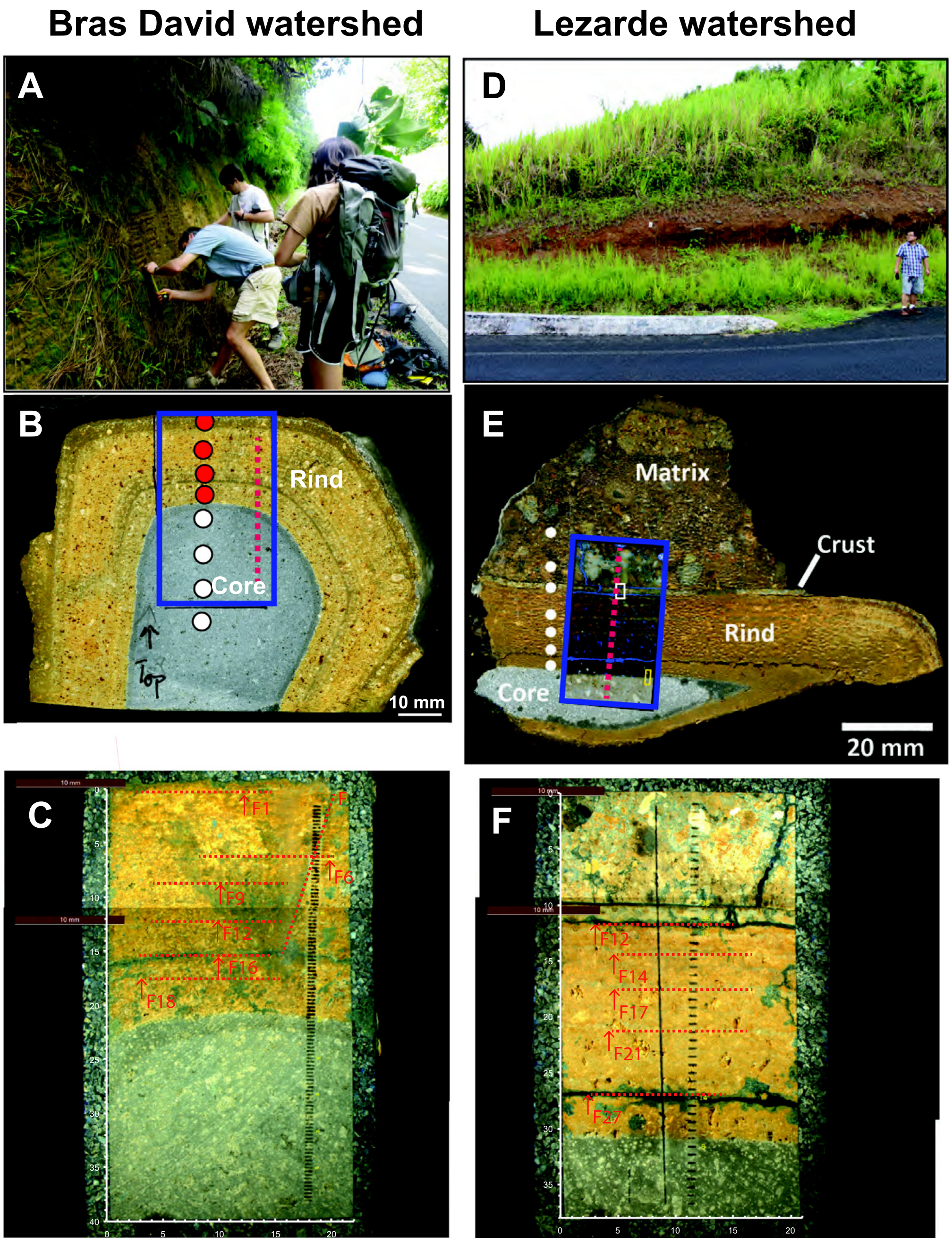

Fig. 2. (a) Field photo of study area in Bras David watershed where clast samples were collected; (b) Photograph of cut sections of the weathering clast from Bras David (BD). The visually defined core-rind boundary is shown. The blue box indicates the location where detailed images and chemical and U-series compositions are measured with the LA MC-ICPMS and LA Q-ICPMS. Drilled sample locations for the core and the rind transects on clast BD are shown as circles (Ma et al., 2012); Red dashed line indicates the locations of LA MC-ICPMS measurements; both dark and light layers indicate the presence of fracture zones in the rind; (c) detailed image of the blue box in (b). The black lines are the locations where LA MC-ICPMS measurements were conducted for U-series disequilibria. The entire area was scanned with LA Q-ICPMS for major and trace element compositions. The fractures observed in Fig. 2B are marked and labeled with their approximate Y locations. (d) Field photo of study area in Lezarde watershed where clast samples were collected; (e) Photograph of cut sections of the weathering clast from Lezarde (AN-14-3.2; Sak et al., 2018). The visually defined core-rind boundary is shown. The blue box indicates the location where detailed images and chemical and U-series compositions are measured with the LA MC-ICPMS and LA Q-ICPMS. Drilled sample locations for the core and the rind transects on clast BD are shown as circles (Sak et al., 2018); Red dashed line indicates the locations of LA MC-ICPMS measurements; both dark and light layers indicate the presence of fracture zones in the rind; (f) detailed image of the blue box in e. The black lines are the locations where LA MC-ICPMS measurements were conducted for U-series disequilibria. The entire area was scanned with LA Q-ICPMS for major and trace element compositions. The fractures observed in (e) are marked and labeled with their approximate Y locations. (For interpretation of the references to color in this figure legend, the reader is referred to the web version of this article.)

Table 1
Study site information.

Watershed Name	Rind Sample	Latitude (DD MM.MMM)	Longitude (DD MM.MMM)	Elevation (m)	MAT (°C)	MAP (mm, TRMM)	Bedrock Age
Bras David	BD	16 10.508 N	61 41.746 W	270	23.3	3840	900 Ka
Lezarde	AN-14-3	16 11.787 N	61 36.326 W	18	24.9	4520	620 Ka
Deshaies	AN-14-7	16 18.635 N	61 46.601 W	281	23.2	1640	1.7 Ma

Table 2
Comparison of U-series isotope compositions for weathering clast core materials measured by LA-MC-ICPMS and solution-based MC-ICPMS.

Name	$(^{238}U/^{232}Th)$	$(^{230}Th/^{232}Th)$	$(^{230}Th/^{238}U)$	$(^{234}U/^{238}U)$
BD core (LA)	1.004 ± 0.075	1.005 ± 0.152	0.997 ± 0.080	0.979 ± 0.059
BD core (bulk)	0.972 ± 0.007	0.970 ± 0.003	0.998 ± 0.005	1.004 ± 0.005
AN-14-3.2 (LA)	0.986 ± 0.101	0.975 ± 0.070	0.993 ± 0.045	0.991 ± 0.039
AN-14-3.2 (bulk)	1.141 ± 0.015	1.016 ± 0.010	0.891 ± 0.015	1.016 ± 0.005

University of Wollongong. Laser ablation was undertaken with a New Wave Research 193 nm ArF excimer laser, equipped with a TV2 cell. A pulse rate of 10 Hz and fluence of 5 J/cm^2 were used. Helium and nitrogen were used together as carrier gas at flow rates of 850 and 10 mL/min, respectively. Ablation was performed along lines 620 μm long with a 150 μm spot size, and a scan speed of 5 μm/sec. Fifty lines were ablated on sample AN-14-3.2, separated by 0.718 mm; and 110 lines on sample BD, separated by 0.330 mm. Before ablation, each line was pre-ablated at a pulse rate of 10 Hz, fluence of 1 J/cm^2, using a spot size of 150 μm and scan speed of 200 μm/sec.

Thorium (^{230}Th, ^{232}Th) and uranium (^{234}U, ^{235}U, ^{238}U) isotopes were measured on a Thermo Neptune Plus multi-collector ICP-MS, equipped with jet sample and x skimmer cones. All five isotopes were collected in static mode, with ^{230}Th and ^{234}U collected in ion counters. Helium flow rate and plasma parameters were tuned with NIST610 element standard to derive a ^{232}Th/^{238}U ratio for this standard greater than 0.8 and thus minimise differences in fractionation between Th and U (Bernal et al., 2006). Measured ^{234}U/^{238}U, ^{230}Th/^{238}U and ^{232}Th/^{238}U isotopic ratios were corrected for elemental fractionation and Faraday cup/SEM yield by comparing measured ratios to those measured on USGS basaltic reference material BCR-2G (Jochum et al., 2005). Background subtraction and calculations of corrected ratios were performed using Iolite™. Accuracy was assessed using USGS basaltic reference material BHVO-2G (Jochum et al., 2005) and NIST glass standard 612 (Stirling et al., 2000). Results of BHVO-2G from the combined two analytical sessions are: $(^{234}U/^{238}U) = 0.989 \pm 0.003$, $(^{230}Th/^{238}U) = 1.018 \pm 0.006$ and $(^{230}Th/^{232}Th) = 1.087 \pm 0.006$ (2SE, N = 24; Appendix Table A1). These values are within error of accepted values for BHVO-2G: $(^{234}U/^{238}U) = 1.00$, $(^{230}Th/^{238}U) = 1.01$ and $(^{230}Th/^{232}Th) = 1.09$ (Mertz-Kraus et al., 2010; Jochum et al., 2005; Matthews et al., 2008). Because there was a systematic shift of $(^{234}U/^{238}U)$ towards lower values in both BHVO-2G and samples compared to solution analyses, an additional correction was undertaken for this ratio using values for BHVO-2G. Such a correction was justified by assessing the corrected $(^{234}U/^{238}U)$ ratio of NIST 612 glass standard: $(^{234}U/^{238}U) = 0.176 \pm 0.001$ (2SE, N = 23; Appendix Table A1), which is comparable to the reference value of $(^{234}U/^{238}U) = 0.1725 \pm 0.0002$ (Stirling et al., 2000).

2.6. In situ LA Q-ICPMS for elemental distribution analysis

In situ elemental analysis was performed by laser ablation quadrupole ICPMS (LA Q-ICPMS) at the Wollongong Isotope Geochronology Laboratory, University of Wollongong. Laser ablation was performed with the same system as above. A pulse rate of 5 Hz and fluence of 0.5 J/cm^2 were used. Helium was used as the carrier gas at a flow rate of 650 mL/min. The entire sample surface was mapped with a spot size of 100 μm, a scan speed of 400 μm/sec and by drawing ablation lines 100 μm apart from each other.

Analytes were measured on a Thermo iCAP-Q single-collector quadrupole ICP-MS, equipped with standard nickel cones and a high sensitivity insert. The following analytes were collected for a total acquisition time of 0.25 sec: ^{23}Na, ^{24}Mg, ^{27}Al, ^{29}Si, ^{39}K, ^{44}Ca, ^{48}Ti, ^{55}Mn, ^{57}Fe, ^{85}Rb, ^{88}Sr, ^{90}Zr, ^{181}Ta, ^{232}Th and ^{238}U. The dwell time on each analyte was 0.01 sec, except for ^{85}Rb, ^{88}Sr, ^{90}Zr, ^{181}Ta (0.02 sec), and ^{232}Th and ^{238}U (0.04 sec). The acquisition time, spot size and scan speed were scaled in order to ensure no distortion of the maps produced (Lear et al., 2012). Each analyte was acquired in normal resolution, except ^{23}Na, ^{24}Mg, ^{27}Al, ^{39}K and ^{48}Ti which were acquired in high resolution because of the high intensities on these nuclides. An interference correction was performed on ^{48}Ti to account for interference from Ca. No drift correction was performed, although it would be possible to implement one by summing the intensities for major elements (Liu et al., 2008). The absence of drift correction would not affect the observations made below. *In situ* reference materials GSC-1G, GSD-1G and GSE-1G from the US Geological Survey (Jochum et al., 2005) were also analyzed before and after each sample. This was undertaken such that a calibration curve could be established and element concentrations determined; however, here we have not calculated element concentrations and simply report analyte intensity heat maps and analyte intensity ratios. Analyte intensities were collected as a function of time, which was converted to x and y coordinates using imaging software developed by Robin Schmid, University of Münster. Heat maps and intensity ratios of measured analytes were then generated in Matlab™.

3. RESULTS

The Bras David weathering clast (Sample BD) contains an unweathered core surrounded by a ~20 to 50 mm thick layer of weathering rind (Fig. 2B). The core of the Bras David sample is porphyritic (Fig. 2C). Previous EMP and XRD analysis indicate that the core composition is andesitic (Sak et al., 2010): the most abundant core material is fine andesitic groundmass and glass matrix; and phenocrysts in the core are generally plagioclase, pyroxene, or ilmenite, with grain sizes ranging from ~10 to 500 μm. The rind material of the Bras David clast has a fine-grained to porphyritic texture. Some phenocrysts were also observed in the rind, including ilmenite, highly altered pyroxene, and highly altered plagioclase. The rind and the core material are separated by a visually defined core-rind boundary based on the contrasting color difference (Fig. 2B).

The weathering clast sample from the Lezarde watershed (AN-14-3.2) consists of an unweathered core and a ~20 mm thick layer of fine-grained weathering rind (Fig. 2E). The outer boundary of rind in AN-14-3.2 is characterized a thin layer of crust (~2 mm) with light yellow to white color that separates the rind from the surrounding soil portion (Fig. 2E). The AN-14-3.2 clast has a porphyritic core with an andesitic composition, similar to the Bras David weathering clast. The core is consisted of fine groundmass, glass matrix, and phenocryts such as plagioclase and pyroxene and the rind is consisted of fine-grained weathered residuals (Sak et al., 2018).

In addition to the fine-grained matrix, the rind portions of both clast samples show presence of fractures that form multiple unusual dark or light color layers (as compared the brown color of the rind matrix) parallel to the core-rind boundary (Fig. 2B and E). The light color of these layers indicates the fracture layer's original color and the dark color resulted from larger fractures filled with wax (dark color) during sample preparation process. Indeed, the same fractures show dark blue color on the thin section billets due to the infilling of blue epoxy (fractures F16, F18 in Fig. 2C, and F27 and F12 in Fig. 2F). The fine fractures with light colors are also marked in Fig. 2 (F1, F6, F9, F12 in Fig. 2C and F14, F17, and F21 in Fig. 2F).

3.1. Elemental maps and core-rind elemental ratio profiles measured by LA Q-ICPMS

For both weathering rind samples, elemental abundances for major and trace elements were characterized by using LA Q-ICPMS to scan the entire section area (~30 mm by 50 mm) that contains both unweathered core and rind materials (Fig. 2C and F). For Ca, Mn, Fe, Al, Si, and U, the relative element abundances (measured as counts per second) were plotted as intensity maps (Fig. 3). As a common feature of in situ spot analysis, the maps show large variability in measured intensities in both the core and the rind materials for the Bras David sample (Fig. 3). Such variability is expected due to relatively larger phenocryst size (~10–500 μm) to the laser spot size used (100 μm), reflecting the porphyritic nature as observed in thin section. Relative to the rind, the core is generally enriched in Ca and Mn but depleted in Fe Al, Si, and U (Fig. 3). In addition, several horizontal layers with distinct color patterns compared to the surrounding areas can be observed in the maps (e.g., the element Ca map; Fig. 3). These layers are located at the same locations as the fractures mentioned above. The presence of fractures obviously affects the measured intensities of the ablated surface. It also can be noted that some bands of very unusual element distribution (horizontal red and blue marks) can be observed in the right edge of the thin section (Fig. 3): these systematic bands are artifacts resulting from the previous *in situ* measurements for U-series isotopes (e.g., black marks in Fig. 2C). To cancel out the possible surface effects on the measured absolute intensity, we calculated the intensity ratio of the traget element to Th, which is generally assumed to be an immobile element (or the least mobile element) during chemical weathering (e.g., Ma et al., 2007, 2012; Engel et al., 2016). To account for the variable nature of the *in situ* analysis, the median of the element/Th ratios was calculated over data from locations $X = 6$ to 23 mm (i.e. in Fig. 3) and then plotted relative to the core-rind boundary as Y location (Fig. 4). A number of general patterns of elements are identified and discussed below.

In general, elements such as Ca and Mn show high element/Th ratios in the core and much lower ratios in the rind materials (the large variability of elemental ratios in the core portion is likely due to the presence of large phenocrysts). Intensity ratios for Ca/Th and Mn/Th show systematical decreasing trends with increasing Y distance from the core to the rind, with a sharp decline in intensity at the visually defined core-rind boundary ($Y = 22.5$ mm, Fig. 4). Element ratios such as Mg/Th, Na/Th, and Sr/Th show a similar trend and are not shown here. These observations indicate that these elements are mobilized and lost during initial water-rock interaction at core-rind boundary. In contrast, elements such as Fe, Al, Si, and U show higher intensity ratios in the rind relative to the core but with different patterns (Fig. 4). The intensity ratios for Fe/Th and Al/Th show a slight increase at the core-rind boundary and the ratios remain relatively constant in rind and then show a large increase in the outmost rind (Fig. 4). The intensity ratio of Si/Th shows a sharp decrease at the core-rind boundary and then a large increase with distance into the outer rind. The intensity ratio of U/Th shows a general increase trend from the core-rind boundary into the rind, with a significant increase at the core-rind boundary and a very gradual increase across the rind.

Element mobility during rind formation has been discussed previously with bulk and electron microprobe

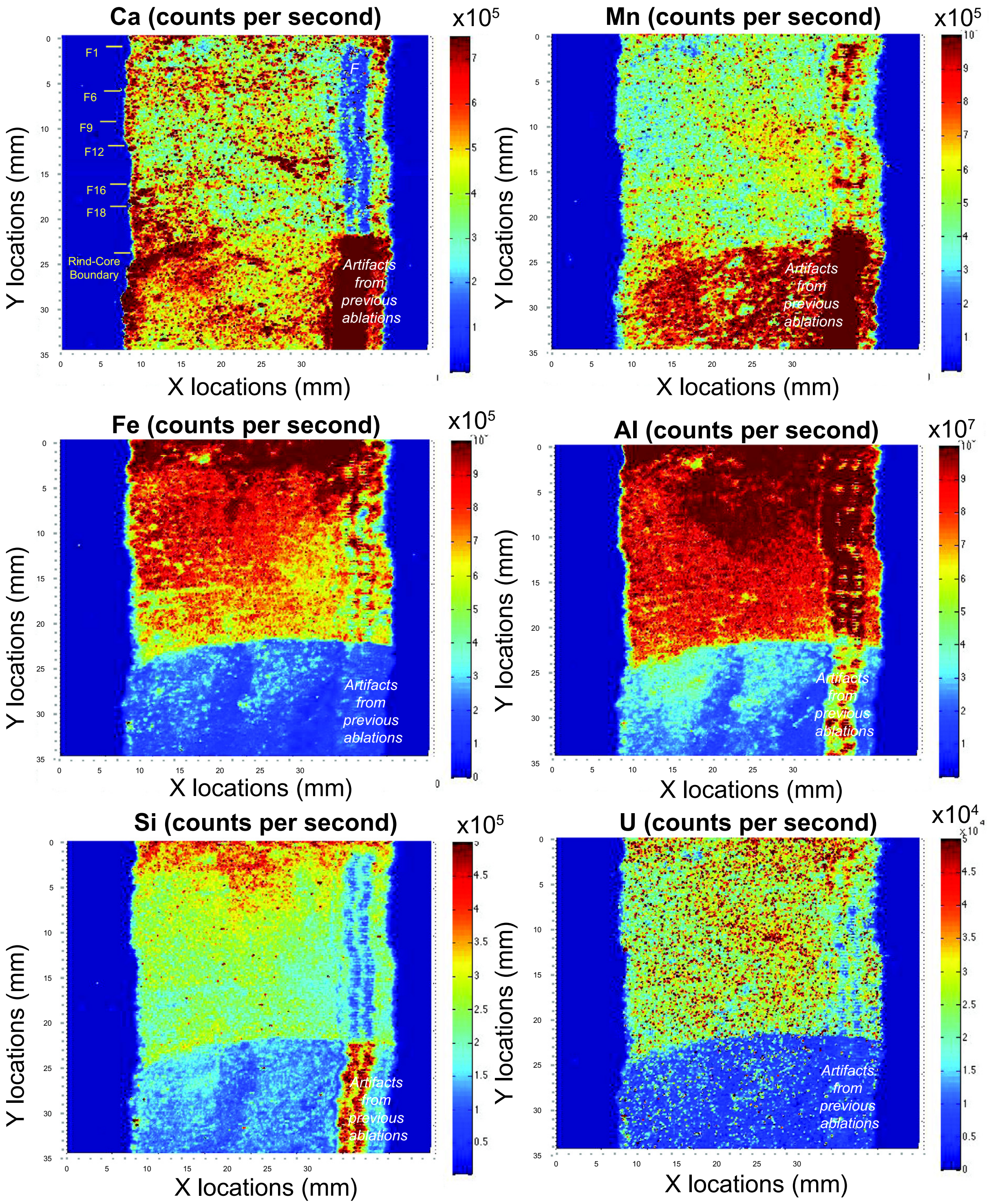

Fig. 3. Intensity maps of LA Q-ICPMS point measurements for elements Ca, Mn, Fe, Al, Si, and U (counts per second) for weathering rind from Bras David watershed (BD), with color ranging from blue to red indicating low to high counts per second. The entire field corresponding to the area in Fig. 2c. Artifacts from previous ablation sites are indicated on the images. Intensity anomalies caused by the fracture zones can also be observed.

measurements along single-line profiles on thin sections for major elements in the Bras David sample (Sak et al, 2010). The LA-Q-ICPMS in situ measurements here provide an improved spatial resolution to study elemental mobility, especially for trace elements such as U that generally have poor detection limits when measured by electron

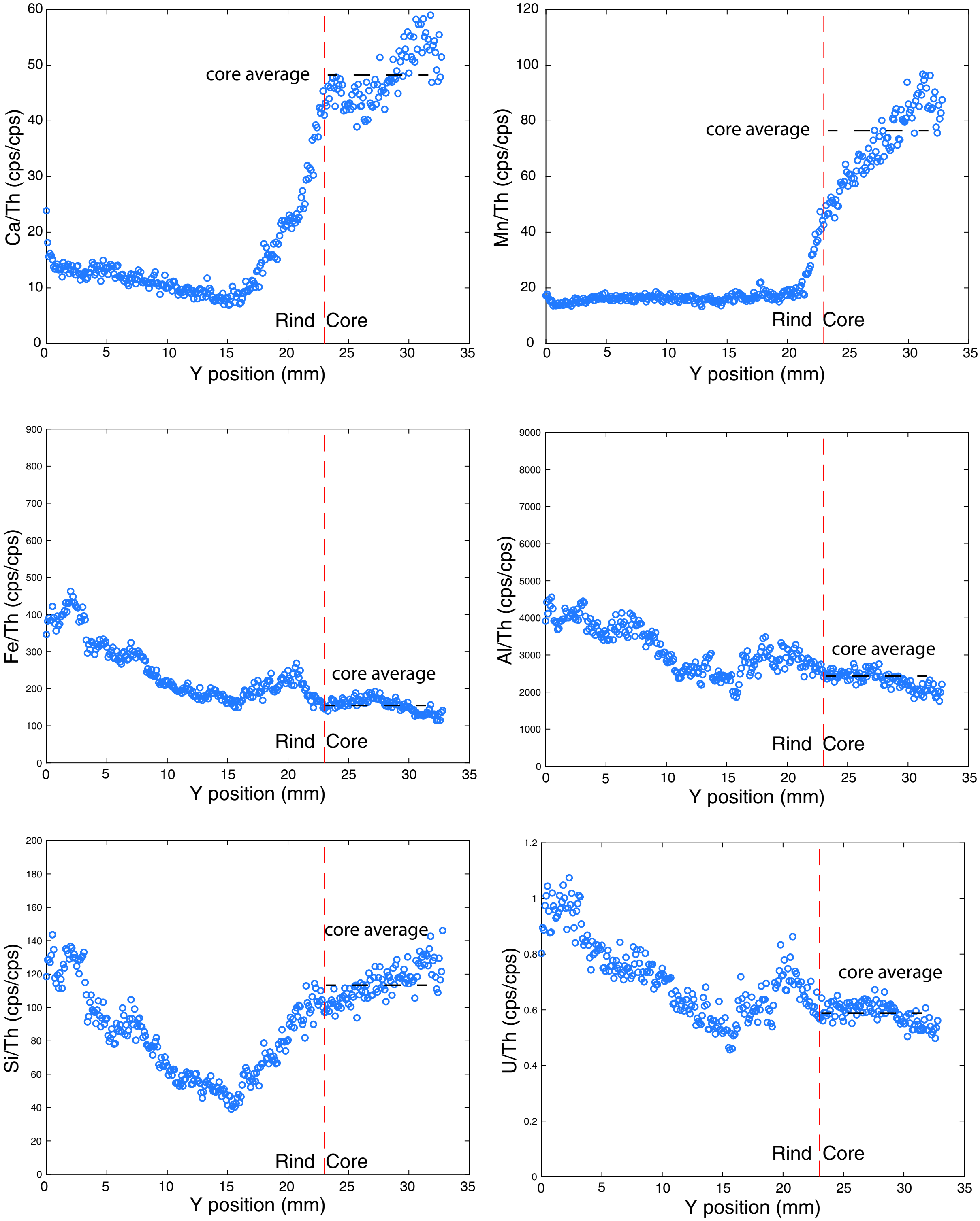

Fig. 4

Fig. 4. Average intensity ratios (cps/cps) for point measurements for Ca/Th, Mn/Th, Fe/Th, Al/Th, Si/Th and U/Th by LA Q-ICPMS on the rind sample (BD) from the Bras David watershed. The Y position indicates locations from core to the rind. Each point is the average values of a group of measurements on locations with X = 6–23 mm (Fig. 3). The dashed line indicates the approximate location of the core-rind boundary.

microprobe. The large number of measurements obtained by LA Q-ICPMS (e.g., over 15,000 measurements for 14 elements over the 30 mm by 50 mm area, as compared to ~10 bulk chemistry measurements) allows for a robust statistical analysis of element distribution, and provide new insights in terms of elemental correlations due to differing mobility behavior during chemical weathering. Indeed, a principal component analysis with the intensity for all measured major and trace elements shows that 63% of the total variance can be accounted for by the first 2 principal components (PC): PC1 = 49% (including elements Fe, Al, U, Si in one cluster, Ti, Th, Zr in one cluster, and Rb, K in one cluster) and PC2 = 15% (with elements Ca, Mn, Mg, and Sr) (Fig. 5). Similarly, a robust variation analysis on the measured intensities shows that variations in U abundance are proportional to those for elements such as Fe, Al, and Si; and variations in Ca abundance are proportional to those for elements such as Mn, Mg, and Sr. Hence, both sets of statistical analyses show consistent results for the elemental profiles revealed by the LA Q-ICPMS analysis.

The relative element/Th ratios for the Lezarde sample (AN-14-3.2) from LA Q-ICPMS measurements show similar trends with respect to elemental mobility during chemical weathering as the Bras David clast.

3.2. Uranium-series disequilibria: *in situ* measurements by LA MC-ICPMS

Uranium-series isotopes were measured with LA MC-ICPMS along transect lines that extend from the unweathered core to the rind, perpendicular to the core-rind interface and with high spatial resolution: at ~0.3 mm spacing for BD and ~0.7 mm spacing for AN-14-3.2 (Appendix Table A2). The laser ablation (LA) markers can be identified visually on the sections after analysis (Fig. 2C and F). The solution-based MC-ICPMS method was previously applied to drilled samples along transects with approximately the same locations as the LA transects (Ma et al., 2012; Sak et al., 2018). For a ~40 mm long transect, the LA method yielded about 50–110 point measurements for U-series disequilibria while the solution method only allowed for ~7 bulk measurements.

3.2.1. Bras David weathering clast

Measured U-series disequilibria by LA MC-ICPMS, shown in this study as U-series activity ratios for ($^{238}U/^{232}Th$), ($^{230}Th/^{232}Th$), ($^{230}Th/^{238}U$) and ($^{234}U/^{238}U$), are consistent with the previously reported U-series disequi-

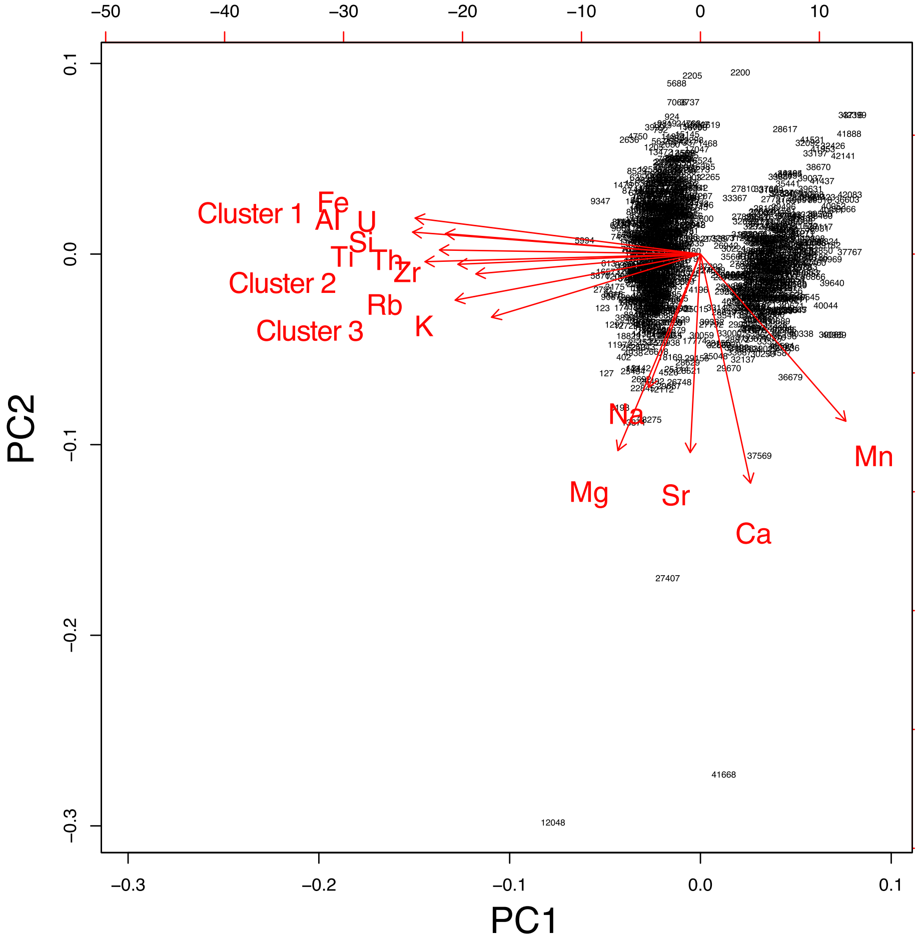

Fig. 5. Principal component analysis (PCA) plot for point measurements for major and trace elements by LA Q-ICPMS on the rind sample (BD: X = 20–60, Y = 0–350 in Fig. 3) from the Bras David watershed.

libria by the solution-based MC-ICPMS method (Ma et al., 2012). The measured (^{238}U/^{232}Th) ratios by LA MC-ICPMS show limited variations across the core portion of the clast, with average (^{238}U/^{232}Th) = 1.004 ± 0.075 (N = 28, 1SD; Table 2). Despite of the relative large uncertainty for LA MC-ICPMS measurements, the core average value is indistinguishable from the bulk average core value measured by solution MC-ICPMS (Fig. 6), with (^{238}U/^{232}Th) = 0.972 ± 0.007 (N = 3, 1SD; Table 2; the comparison passes a t test with p = 0.84). The rind portion analyzed by LA shows (^{238}U/^{232}Th) values that increase gradually with distance from the core-rind boundary into the weathering rind (Fig. 6). This trend is confirmed by the values measured by solution MC-ICPMS (Ma et al., 2012).

Similarly, (^{230}Th/^{232}Th) ratios measured by LA MC-ICPMS (Fig. 6) are generally consistent with solution MC-ICPMS measurements (Ma et al., 2012). The average (^{230}Th/^{232}Th) value of the core portion is 1.005 ± 0.152 by LA (N = 28, 1SD; Table 2), in agreement with the solution value 0.970 ± 0.030 (N = 3, 1SD; passing t test with p = 0.70), considering the relatively large error on LA measurements. The (^{230}Th/^{232}Th) values of the rind portion measured by LA-MC-ICPMS show a slightly increasing trend from the core-rind boundary into the rind (Fig. 6), similar to the previous increasing trend observed by the solution MC-ICPMS (Ma et al., 2012).

Uranium-series disequilibria are also evaluated using (^{230}Th/^{238}U) and (^{234}U/^{238}U) ratios (Fig. 6). The (^{230}Th/^{238}U) and (^{234}U/^{238}U) ratios measured by LA MC-ICPMS show limited variation in the core portion of the sample, with average values of 0.997 ± 0.080 (N = 28, 1SD) and 0.979 ± 0.059 (N = 28, 1SD), respectively (Table 2). These values are consistent with solution MC-ICPMS measurements: 0.998 ± 0.005 (N = 3, 1SD) and 1.004 ± 0.005 (N = 3, 1SD and passing t test with p = 0.48), respectively. Laser ablation MC-ICPMS data show that a decrease in (^{230}Th/^{238}U) ratios from the core-rind boundary into the rind (Fig. 6), also similar to the decreasing trend observed by solution MC-ICPMS (Ma et al., 2012).

It is noted that several data points of unusual LA U-series ratios (as compared to the general LA data trends) with large measured error bars are located near the previously identified fractures (such as F1, F6, F12, and F16 in Fig. 2C), suggesting that these materials in the fractures have different U-series isotope compositions as compared to the rind matrix materials.

3.2.2. *AN-14-3.2 weathering clast*

For sample AN-14-3.2, measured U-series isotope disequilibria by LA MC-ICPMS (Fig. 6) are consistent with solution MC-ICPMS measurements (Sak et al., 2018). In particular, core average values for the LA-MC-ICPMS data are: (^{238}U/^{232}Th) = 0.986 ± 0.101 (N = 9, 1SD), (^{230}Th/^{232}Th) = 0.975 ± 0.070 (N = 9, 1SD), (^{230}Th/^{238}U) = 0.993 ± 0.045 (N = 9, 1SD), (^{234}U/^{238}U) = 0.991 ± 0.039 (N = 9, 1SD) (Table 2), in general agreement with solution MC-ICPMS results: (^{238}U/^{232}Th) = 1.141 ± 0.015 (N = 1, 1SD), (^{230}Th/^{232}Th) = 1.016 ± 0.010 (N = 1, 1SD), (^{230}Th/^{238}U) = 0.891 ± 0.015 (N = 1, 1SD), (^{234}U/^{238}U) = 1.016 ± 0.005 (N = 1, 1SD), considering the relatively large error bars of the LA-MC-ICPMS results.

For the rind portion of sample AN-14-3.2, (^{238}U/^{232}Th) ratios show an increasing trend from the core-rind boundary into the rind, and then change to lower values across the rind-crust boundary (Fig. 6). (^{238}U/^{232}Th) ratios in the soil portion of the thin section show very large variations. (^{230}Th/^{232}Th) ratios by LA MC-ICPMS show slightly increasing trends from the core to the rind (Fig. 6), a trend that is also observed in the bulk measurements. In addition, (^{230}Th/^{232}Th) ratios of the crust portion show lower values than the rind and (^{230}Th/^{232}Th) ratios of the soil portion show very high values with large variations, similar to the trends observed by the (^{238}U/^{232}Th) ratios (Fig. 6). (^{234}U/^{238}U) and (^{230}Th/^{238}U) ratios measured by the LA MC-ICPMS also mimic the trends as observed in the bulk measurements (Fig. 6).

It is also noted that several data points of unusual LA U-series ratios (as compared to the general LA data trends) with large measured error bars are located near the previously identified locations of fractures (such as F12, F14, and F21 in Fig. 2F), suggesting that materials in the fractures have different U-series isotope compositions as compared to the rind matrix materials.

To summarize, the LA data accurately reproduce the solution MC-ICPMS data, albeit with a relative poor precision due to the nature of the *in situ* measurements. *In situ* measurements confirm the previous observations in the bulk measurements (Ma et al., 2012; Sak et al., 2018), that is: (1) the cores of the weathering clasts are homogenous in terms of U-series isotope compositions; and (2) the rind portions show systematically increasing (^{238}U/^{232}Th) and (^{230}Th/^{232}Th), and decreasing (^{230}Th/^{238}U) ratios with increasing distance into the rind from the core-rind boundary.

4. DISCUSSION

4.1. Formation of weathering rinds

Weathering rinds from Basse-Terre Island have been previously characterized in detail to provide insights into chemical weathering processes such as the sequence of weathering reactions, elemental mobility, porosity development, and controls of core-rind interface curvature and environmental conditions on rind thickness and weathering rates (Sak et al., 2010; Ma et al, 2012; Lebedeva et al., 2015; Engel et al., 2016). The LA techniques used here not only provide additional information that confirms the previous observations of rind formation processes (i.e., weathering reaction sequence, elemental mobility, and porosity development), but also reveal new details of processes that occur across the core-rind boundary such as initiation of weathering reactions.

The weathering rind portions of both samples (BD and AN-14-3.2) show enrichment of elements such as Fe, Al, Si, and U, and significant depletions of elements such as Ca, and Mn, relative to core compositions (Figs. 3 and 4). These element distribution patterns have been previously

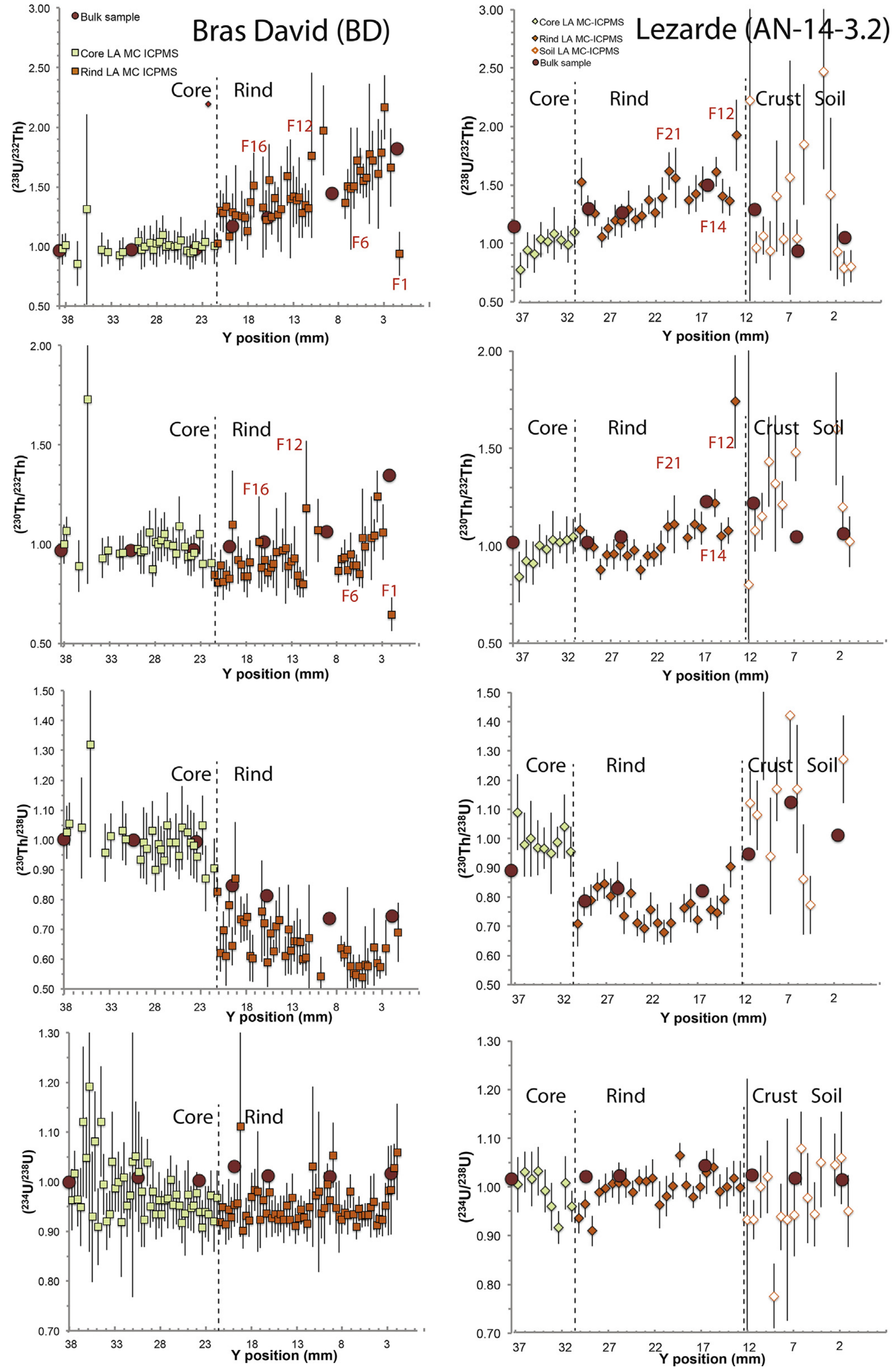

Fig. 6. Measured U-series activity ratios: (^{238}U/^{232}Th), (^{230}Th/^{232}Th), (^{230}Th/^{238}U), (^{234}U/^{238}U) plotted as a function of distance relative to the core–rind boundary for the two weathering clast samples. Results from LA MC-ICPMS (squares and diamonds with error bars) and bulk U-series isotope analysis (large red circles) are shown for the core, rind (BD) and the core, rind, crust, and soil matrix (AN-14-3.2). The LA MC-ICPMS transects were measured perpendicular to the core-rind boundary: each step on the BD sample is equivalent to 0.33 mm and each step on the AN-14-3.2 samples is equivalent to 0.72 mm. Areas where micro-fractures and core-rind, rind-crust, and crust-soil boundaries were observed on thin sections are also indicated. (For interpretation of the references to color in this figure legend, the reader is referred to the web version of this article.)

interpreted for the case of Basse-Terre Island as the weathering sequence of the basaltic-andesitic core material including dissolution of plagioclase, pyroxene, groundmass matrix, and glass materials that start near the core-rind boundary, as well as accumulation of secondary weathering products such as Fe-Al hydroxides, secondary clay minerals in the rind (Sak et al., 2010, 2018). The LA results provide the high spatial resolution required to understand elemental changes and associated weathering reactions across the narrow reaction front at the core-rind boundary. For example, the LA elemental profiles show a narrow and abrupt reaction boundary (Fig. 4) for all elements listed above. These reaction fronts coincide with the visually-defined core-rind boundary (Fig. 4). Indeed, the LA-derived Ca and Mn profiles suggest that the loss of Ca occur at the visually-defined core-rind boundary and, however, the loss of Mn occurs prior to the loss of Ca, with its reaction front located coreward within ~1.5 mm of core-rind boundary (Fig. 4). This suggests that Mn-bearing minerals (such as pyroxene) start to weather in the core prior to major Ca-bearing minerals (such as plagioclase). It has been hypothesized that diffusion of oxygen in pore fluids across the core-rind boundary leads to oxidation of Fe(II)-bearing minerals in the core and thus the increase in mineral volumes plays an important role for porosity development during weathering initiation (Buss et al, 2008; Navarre-Sitchler et al., 2011). Such a redox-controlled and oxygen diffusion weathering mechanism at the core-rind boundary is consistent with the early release of Mn from pyroxene weathering (Fig. 4). Indeed, the first reaction identified in the core of the Guadeloupe clast is oxidation of Fe in pyroxene (Sak et al., 2010).

Significant porosity is generated only when plagioclase dissolution begins, slightly further rindward at the core-rind interface as shown by the Ca profile (Fig. 4). Further development of porosity at the core-rind boundary (coreward) leads to more pore fluid-core interaction and weathering of plagioclase and groundmass materials, as observed for rapid Ca release across the core-rind boundary (Fig. 4). The abrupt loss of Ca at the core-rind boundary is accompanied by the first initial release of Si rindward of the core-rind boundary (Fig. 4). The Si/Th intensity ratios start to decrease as weathering proceeds in the rind at distances of ~0.5 mm from the boundary: specifically, Si is inferred to become relatively mobile within ~10 mm of the boundary (Fig. 4). The Si/Th starts to increase in the outer part of the rind, suggesting the addition of Si in the outer part of the weathering rind. Such an increase could be due to the addition of dissolved Si from infiltrating soil water to the surface of altered minerals in the outer rind. Indeed, using Si and O isotope spikes, several studies have shown that a large portion of Si in layers at the surface of altered minerals or glass materials can derive from the aqueous phase (Valle et al., 2010; Verney-Carron et al., 2008).

The diagnostic brownish yellow color of the weathering rind that distinguishes the weathering rind from the surrounding regolith (Fig. 2F) can be attributed to iron oxide phases such as goethite, α-FeO(OH), that form through weathering reactions in lateritic soils (Sak et al., 2018). The dissolution of the pyroxene, ilmenite, and groundmass + glass phases in the core produce $FeO(OH)_{(s)}$ and $Fe^{2+}_{(aq)}$ and as the weathering reaction front advances coreward, the FeO(OH) precipitates accumulate in the rinds. Similarly, the Al released from weathering of the core material accumulate in the rinds as Al hydroxides. Indeed, intensity ratios of Fe/Th and Al/Th in inner rinds show values that are similar to (or slightly higher) than the intensity ratios of the core materials (Fig. 4). This is consistent with Fe and Al accumulating in the rind as Fe-Al hydroxides when primary minerals and glass materials weather. The slightly elevated Fe/Th and Al/Th ratios in this rind portion (within ~10 mm from core-rind boundary) could be due to local heterogeneity or slight mobility of Th. However, both Fe/Th and Al/Th ratios are significantly elevated for the outer rind (~10–22 mm from the core-rind boundary), similar to the Si/Th ratios, and suggest that both Fe and Al might be accumulating in the outer rind from external sources that are related to infiltrating soil waters. Such local-scale redistribution of Fe and Al could be consistent with the increase in mobility of Fe and Al during formation and transformation of secondary Fe and Al minerals under extreme tropical weathering conditions (e.g., Ma et al., 2007; Buss et al., 2010; Clergue et al., 2015). For example, it is possible that Fe and Al are not mobile in the innermost rind, but in the outer rind near the soil fluids, mobility is more likely.

Indeed, the addition of Fe to weathering rinds and the pronounced Fe mobility is also supported by bulk chemistry analysis of multiple weathering rind samples from Basse-Terre Island (Ma, 2018).

Uranium exhibits an addition profile (U/Th intensity ratios in Fig. 4) in the weathered rind, suggesting input of U from the regolith/soil matrix into the rind. Uranium addition profiles have been observed in the previous studies of weathering rinds developed under tropical climates (Pelt et al., 2008; Ma et al., 2012; Engel et al., 2016). It has been proposed that soil water that percolates through rind matrix may contain mobile U(VI) that can subsequently adsorb to or be incorporated into Fe-hydroxides (Pelt et al., 2008; Ma et al., 2012; Engel et al., 2016). Those previous studies relied on the observed addition profile of U, constructed with the bulk measurements of drilled samples (e.g., ~10 samples along the profile). In this study, the large number of LA Q-ICPMS measurements (~15,000 measurements) offers a powerful and quantitative mean to understand U mobility. Statistical analyses (PCA component and correlation matrixes) of all elements show that the presence of U in the weathering rind is highly correlated with elements such as Fe and Al (Fig. 5). This observation is consistent with the previous hypothesis that U mobility in the rind is largely controlled by adsorption or incorporation into Fe-hydroxides.

4.2. Behavior of U-series isotopes during rind formation

Uranium-series disequilibria in weathering rinds and profiles have been used to quantify weathering duration and rates (e.g., review by Chabaux et al., 2003, 2008; Dosseto, 2015). The U-series disequilibria result from chemical weathering processes due to the different mobility of U-series isotopes. Thorium is generally immobile and particle-reactive during water-rock interaction and U is highly mobilized during water-rock interactions under oxidizing conditions (e.g., Rosholt et al., 1966; Latham and Schwarcz, 1987a,b; Gascoyne, 1992; Chabaux et al., 2003). This normally leads to high U/Th elemental ratios in natural water and low U/Th ratios in weathering residuals. However, high U/Th ratios due to U addition and subsequent immobilization has been observed in weathering rinds (Pelt et al., 2008; Ma et al., 2012; Engel et al., 2016), as well as soil profiles (Dequincey et al., 2002; Chabaux et al., 2003; Dosseto et al., 2008b; Ma et al., 2010), and river sediments (Andersson et al., 1998; Dosseto et al., 2006; Granet et al., 2007, 2010). As discussed in Section 4.1, U addition in rinds was interpreted as U precipitated or adsorbed onto secondary Fe-hydroxides or clay minerals from soil pore waters (Ames et al., 1983; Shirvington, 1983; Andersson et al., 1998; Duff et al., 2002; Chabaux et al., 2003, 2008 and references therein). Uranium immobilization is also likely when infiltrating pore waters become reducing because solubility of U-containing phases are lower under those conditions (Chabaux et al., 2003, 2008 and references therein).

The LA MC-ICPMS measurements show U-series disequilibria with a high spatial resolution, at ~300–700 μm spacing along ~35 mm long transects for both weathering clasts (Fig. 6). These *in situ* measurements reveal systematic trends of U-series disequilibria consistent with the bulk measurements from solution MC-ICPMS. The observed (^{234}U/^{238}U) activity ratios in the weathering products (i.e., the rind) show disequilibrium (Fig. 6), with values both greater and less than one. This observation is consistent with addition of U (as evidenced by high U/Th ratios in rinds) as a precipitate or sorbate from soil pore waters during rind formation. Due to the preferential release ^{234}U over ^{238}U during water-rock interaction (Fleischer, 1980), fluid phases are generally characterized by (^{234}U/^{238}U) activity ratios >1 while residual solid materials that have recently weathered are generally characterized by (^{234}U/^{238}U) activity ratios <1 (e.g., Rosholt et al., 1966; Vigier et al., 2001; Chabaux et al., 2003, 2008; Dosseto et al., 2008a; Andersen et al., 2009). The presence of (^{234}U/^{238}U) ratios <1 in rinds also reveal the dual process of U mobility in rinds (e.g., Dequincey et al., 2002): both U addition and U loss occur during rind formation. The addition of ^{238}U is also responsible for the observed increase of (^{238}U/^{232}Th) and decrease of (^{230}Th/^{238}U) ratios in both transects in the rind of both samples (Fig. 6). Over time, subsequent production of ^{230}Th from excess ^{234}U in the rind accounts for the observed increase of (^{230}Th/^{232}Th) activity ratios in both transects (Fig. 6).

The LA MC-ICPMS measurements also reveal U-series disequilibria in detail for locations near the core-rind boundary, which is not available from the previous bulk measurements. At the visually-defined core-rind boundary, (^{238}U/^{232}Th) activity ratios show a large and abrupt increase just a few hundreds μm rindward of the boundary in both clasts (Figs. 6 or 4). Such a step-wise increase in (^{238}U/^{232}Th) ratios at the boundary is different from the more gradual increase trend of (^{238}U/^{232}Th) ratios in the rest of rind. Similar abrupt increases in (^{238}U/^{232}Th) ratios are also observed coincident with several fractures in the rind (e.g. fracture F18, F16, F12, F9 in Fig. 6). This changes reflect an abrupt process that added U rapidly to these locations, in additional to the continuous and gradual U addition process that occurred in the rind matrix. These locations coincide with areas where large fractures are observed (e.g., at the visually-defined core-rind boundary as well as other fracture zones in Fig. 2C and F). The presence of fractures leads to large increases in porosity and permeability in these areas compared to non-fractured rind matrix areas. The increases in porosity and permeability could change the transport mechanisms for pore waters in these regions and hence changes the rates that U was added at these fracture locations.

Similarly, abrupt changes are also observed for (^{230}Th/^{238}U), (^{230}Th/^{232}Th), and (^{234}U/^{238}U) ratios in these same locations that can also be similarly attributed to the impact of local fractures at these locations (Fig. 6). Indeed, the relatively lower (^{234}U/^{238}U) and (^{230}Th/^{232}Th) ratios at several fracture locations may also suggest the presence of an extensive leaching process that removed ^{234}U and hence its decay product ^{230}Th. In combination with the high (^{238}U/^{232}Th) and low (^{230}Th/^{238}U) ratios that suggest extensive U addition, both enhanced U addition and U loss are observed near the fractures. Such a dual-process of U mobility has been previous discussed in weathering rind studies (Ma et al., 2012; Engel et al., 2016).

Large variability of U-series disequilibria is observed in the crust and soil portions of sample AN-14-3.2 from the Lezarde watershed (Fig. 6). The crust is the physical boundary between the weathering rind and the surrounding matrix material and marked as an indurated crust, bordered by Fe and Mn enrichment (Sak et al., 2018). This crust layer is marked with abrupt changes in elemental concentrations of Mn, Al, Ba, Si, and Mg. The preservation of the rind-soil interface permits characterization of weathering reactions and material exchanges between the weathering clast (core and rind), and the surrounding soil matrix for clast AN-14-3.2, shedding insights into communication between the enveloping weathering rind and host regolith (Sak et al., 2018). For this study we focus on the LA data from the rind and the core.

To summarize, for both weathering rind systems, in situ measurements of (^{238}U/^{232}Th) and (^{230}Th/^{232}Th) activity ratios increase across the core-rind boundary into the rind (Fig. 6). The influx of soil water that carries dissolved U is readily explained by the increase in bulk porosity in the rind matrix during chemical weathering of core materials. Absorption or co-precipitation of U from soil water is likely as secondary Fe-hydroxides and clay minerals are observed to be abundant in the rind (Sak et al., 2010).

4.3. Rind formation rates calculated from ^{238}U-^{234}U-^{230}Th disequilibria

The conservative behavior of Th isotopes and mobile behavior of U isotopes (loss and addition) allow for modeling of U-series disequilibria as a function of time during rind formation (Pelt et al., 2008; Ma et al., 2012; Engel et al., 2016). Under open-system conditions for U-series mobility, the U-series isotopic variations in the rind over time can be modeled as (Dequincey et al., 2002; Ma et al., 2012; Engel et al., 2016):

$$\frac{d^{238}U}{dt} = f_{238} - \lambda_{238}^{238}U - k_{238}^{238}U \quad (1)$$

$$\frac{d^{234}U}{dt} = f_{234} + \lambda_{238}^{238}U - \lambda_{234}^{234}U - k_{234}^{234}U \quad (2)$$

$$\frac{d^{230}Th}{dt} = \lambda_{234}^{234}U - \lambda_{230}^{230}Th \quad (3)$$

$$\frac{d^{232}Th}{dt} = -\lambda_{232}^{232}Th \quad (4)$$

Here, ^{238}U, ^{234}U, ^{230}Th, and ^{232}Th refer to the U-series nuclide concentrations in the rind (atoms g^{-1}); f_{238} and f_{234} are respectively the input rates of ^{238}U and ^{234}U into the rind (atoms g^{-1} yr^{-1}). The f terms are assumed to lump together all the processes that add significant amounts of U-series isotopes into the rind material (adsorption, precipitation, and incorporation), except radioactive production and decay. The parameters k_{238} and k_{234} are first-order weathering rate constants (yr^{-1}) for release of ^{238}U and ^{234}U, respectively, from U-containing phases from the rind (Latham and Schwarcz, 1987a,b; Plater et al., 1992; Vigier et al., 2001), i.e. the rates that U-containing phases dissolve equal k_{238}. ^{238}U or k_{234}.^{234}U. In the model, the f and k terms are considered to be constant with time for the purpose of simplicity and tractability (Ghaleb et al., 1990; Dequincey et al., 2002). Previous studies have shown a close-to-linear increase of (^{238}U/^{232}Th) ratios with distance from the core into the rind (Ma et al., 2012; Engel et al., 2016) that is consistent with a constant ^{238}U input rate in the model. Terms λ_{238}, λ_{234}, λ_{230}, and λ_{232} are the decay constants for ^{238}U, ^{234}U, ^{230}Th and ^{232}Th, respectively (yr^{-1}).

For a given sample, we model the rind formation age, t (in years). This age represents the onset of water-mineral interaction that creates U-series disequilibrium. Spatially, the onset of disequilibrium occurs at the core-rind boundary. Disequilibrium increases into the rind, and with it the rind formation age. The term ($\lambda_{234}f_{234}$)/($\lambda_{238}f_{238}$) represents the (^{234}U/^{238}U) activity ratio of the input source, e.g., the soil pore water. The term, k_{234}/k_{238} describes the relative loss of ^{234}U to ^{238}U during leaching. Thus, the k_{234}/k_{238} ratio documents the preferential release of ^{234}U into solution due to alpha particle damage to the crystal lattice (k_{234}), compared to the congruent release of ^{234}U and ^{238}U during mineral dissolution (k_{238}).

Due to the nature of the variability of *in situ* measurements, a 6-point moving average algorithm was used to smooth the U-series data reported by LA MC-ICPMS as well as to minimize the effects of heterogeneity of the core and rind materials (Fig. 7). The moving average points mimic the *in situ* measurements, with similar trends to those observed in bulk measurements (Fig. 7). It is noted that the bulk samples were from drilled pits with a diameter of ~3.5 mm and the LA spacing size is about 0.3–0.7 mm. The 6-point moving average LA samples hence yield a spatial resolution equivalent to a bulk sample size varying between 1.8 and 4.2 mm, comparable to the spatial resolution of bulk measurements, but with a much larger number of data points (~60 points for BD and ~30 points for AN-14-3.2, compared to <10 bulk measurements).

With the moving average points of (^{238}U/^{232}Th) and (^{230}Th/^{232}Th) activity ratios in weathering rinds as input values, and the core U-series activity ratios at the core-rind boundary as initial conditions (Table 3), the unknown parameters (f_{238}, f_{234}, k_{234}, k_{238} and t) are fully solved by using a Monte Carlo inverse algorithm (Engel et al., 2016). The model-derived parameters are presented in Table 3. The model calculations show both (^{238}U/^{232}Th) and (^{230}Th/^{232}Th) ratios increase with rind formation ages (Fig. 7), consistent with the input ratios in rind samples for each profile (BD model results have a more pronounced increase trend of (^{238}U/^{232}Th) and (^{230}Th/^{232}Th) ratios than the AN-14-3.2 model, because the observed changes of ^{230}Th/^{232}Th in BD rind samples are larger than in the AN-14-3.2 rind samples). It is noted that the inner core in both clasts (the least likely weathered materials) show different U-series compositions compared to the core near the core-rind boundary, suggesting the initial weathering processes have already modified materials coreward of the core-rind boundary prior to the formation of rind (Section 4.2). Furthermore, the rind formation ages for the two transects generally increase with distance away from the core-rind boundary (Fig. 8), consistent with the previous model results based on the bulk measurements (Ma et al., 2012; Sak et al., 2018). Several rind samples show much older ages as compared to the general increasing age-distance trends (Fig. 8). These samples yielding older ages are located near known fractures on the rind and possibly show the influence of fractures on U-series mobility, yielding anomalous large disequilibria (also see Section 4.4). Modeled k_{238}, k_{234}/k_{238}, f_{238} and f_{234}/f_{238} values from the two rind profiles (Table 3) are comparable to the modeled parameters from bulk measurements (Ma et al., 2012; Sak et al., 2018). In general, these parameters are within the range of U-series constants from weathering profiles or river sediments (Dosseto et al., 2008a,b; Ma et al., 2010, 2012; Vigier et al., 2001; Dequincey et al., 2002; Andersen et al., 2009).

4.4. Rind formation rates

In both clasts, rind formation ages increase with distance away from the core-rind boundary into the rind (Fig. 8). Despite the large scatter on the age-distance relationship of the *in situ* measurement results, the age-distance trend yields a rind formation rate of 0.19 ± 0.03 mm/kyr for the Bras David clast, and 0.29 ± 0.11 mm/kyr for the Lezarde clast (AN-14-3.2). These in situ rates are consistent with the previously estimated rind formation rates from bulk measurements: 0.18 ± 0.07 mm/kyr for the Bras David rind (Ma et al., 2012) and 0.21 ± 0.15 mm/kyr for the Lezarde rind (Sak et al., 2018), respectively. The first order comparison of these rates shows that *in situ* U-series measurements can provide reliable U-series disequilibria for modeling and yield rind formation rates consistent with those constrained by con-

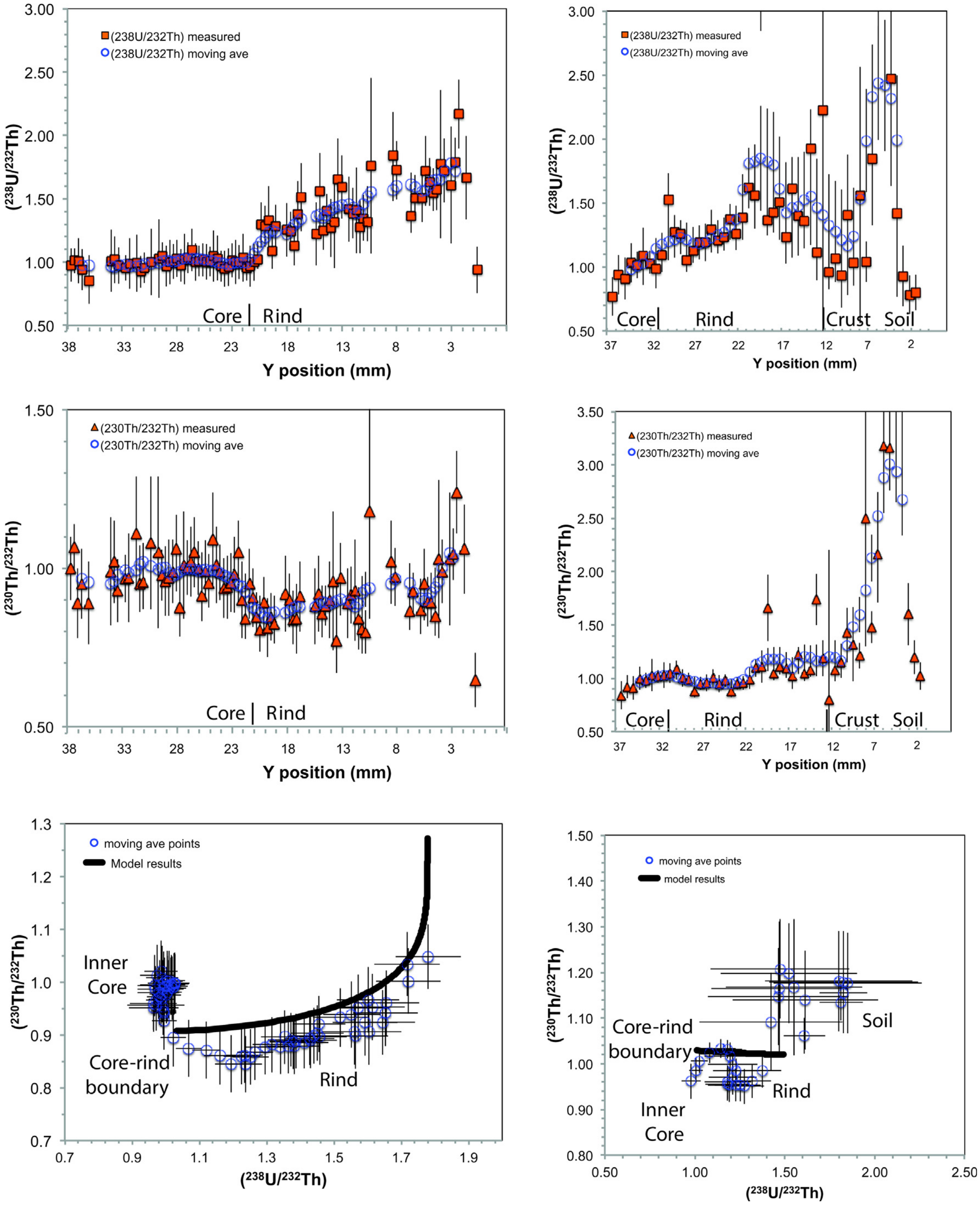

Fig. 7. Measured U-series activity ratios: (^{238}U/^{232}Th); (^{230}Th/^{232}Th) plotted as a function of distance relative to the core–rind boundary for the two weathering clasts: BD and AN-14-3.2. The measurements were done by LA MC-ICPMS. The blue circles indicate the 6-point moving averages of the raw measurements. The 6-point moving averages for (^{230}Th/^{232}Th) and (^{238}U/^{232}Th) were plotted on the isochron diagram with the estimated uncertainties, along with the U-series mobility model curves (black lines). The U–Th radioactive disequilibrium of the weathering rind samples is explained by (1) continuous gain and loss of U starting at the core–rind boundary (without gain or loss of Th), and (2) subsequent production of ^{230}Th from U-series decay series in the rind. Rind formation ages were determined using an open-system U gain-loss model (see text for details). Modeled (^{238}U/^{232}Th) and (^{230}Th/^{232}Th) activity ratios (using parameters in Table 3) are shown as black curves. (For interpretation of the references to color in this figure legend, the reader is referred to the web version of this article.)

Table 3
Rind formation rates and model parameters determined from U-series disequilibria.

Rind Sample	$f_{238U}/^{238}U_0$ (yr^{-1})	f_{234U}/f_{238U}	k_{238U} (yr^{-1})	k_{234U}/k_{238U}	Rind formation rates, linear law (mm/kyr)	R^2 (linear law)	Rind age-distance equation (power law)	R^2 (power law)
Bras David (In situ LA, this study)	$7.06 \pm 2.84 \times 10^{-5}$	1.25 ± 0.14	$3.98 \pm 1.67 \times 10^{-5}$	1.77 ± 0.18	0.19 ± 0.03	0.16	D (mm) $= 0.00067\,t^{0.90}$ (yr)	0.61
Bras David (Bulk, Ma et al., 2012)	2.5×10^{-5}	1.07	1.2×10^{-5}	1.07	0.18 ± 0.07	0.87		
Lezarde AN-14-3.2 (In situ LA, this study)	$7.05 \pm 2.72 \times 10^{-5}$	1.23 ± 0.09	$4.67 \pm 1.88 \times 10^{-5}$	1.82 ± 0.13	0.29 ± 0.11	<0	D (mm) $= 0.0156\,t^{0.65}$ (yr)	0.57
Lezarde AN-14-3.2 (Bulk, Sak et al., 2018)	$7.8 \pm 1.6 \times 10^{-5}$	1.09 ± 0.04	$5.9 \pm 1.2 \times 10^{-5}$	1.05 ± 0.05	0.21 ± 0.15	0.85		

ventional bulk U-series measurements, with the tremendous advantage to provide fast sample throughput and generate large numbers of U-series analyses.

The weathering rind formation ages derived from the *in situ* measurements show a large degree of scatter as a function of distance (Fig. 8). For example, the correlation coefficients for the linear fits are low ($R^2 < 0.2$ for both weathering clasts) while the rind formation rates derived from bulk measurements in previous studies yielded better linear fits ($R^2 = 0.8$ to 0.9; Ma et al., 2012; Sak et al., 2018). This apparent discrepancy of the two linear fits may be attributed to two reasons. First, *in situ* measurements provide a high spatial resolution for the age-distance relationship at sub-mm spacing compared to bulk measurements at several mm spacing, and reveal the possible influence of micro-structures on weathering processes in rinds. Indeed, large variations of rind formation ages are generally observed in locations with presence of fractures where large variability of in situ U-series disequilibria has been observed (Fig. 8). As stated above, the mobility of U-series isotopes in these fine fractures is probably different from mobility in the rind matrix. For example, calculated rind formation ages located at the fractures are unusually old compared to the ages in nearby rind matrix (Fig. 8). We interpret this observation as the limitation of the U-series model that considered all data input (rind matrix vs. fractures) equally and the derived model parameters hence reflect the average conditions for the entire rind (as if it were a homogeneous porous media with similar porosity everywhere) and ignore the variability potentially related to the fractures. Hence, unusually old formation ages at the fractures likely indicate that the fluxes of U leaching and addition were underestimated with the current model (Fig. 8). A future model system that differentiates U-series behavior in the general rind area from that of fracture locations might be a better approach to solve this issue. At this stage of model interpretation, we simply ignore the unusually old rind ages at the fractures when considering the age-distance relationship (Fig. 8).

Secondly, the large number of data points obtained by the *in situ* measurements allow for a detailed evaluation of the age-distance relationship, instead of a simple linear relationship. In the previous studies (Pelt et al., 2008; Ma et al., 2012; Engel et al., 2016; Sak et al., 2018), a linear fit was used to derive a rind formation rate that implies that the formation rates remain constant throughout the entire weathering duration. Although the linear rate law is a common approach used to describe the long-term average rind formation rate, numerical model evaluations with a weathering system dominated by diffusive transport (e.g., in the weathering rind) has shown that even if transport velocity and fluid velocities are identical at the scale of a single pore, as transport distances increase, the solute velocity diminishes approximately as a power law (e.g., Lebedeva et al., 2015; Hunt, 2015; Hunt and Sahimi, 2017). The rind thickness, or the distance to the core-rind boundary (D), may increase as a sub-linear power law of the rind formation age (t), $D = A \times t^s$, (both A and t are fitting constants, with predicted values of s between 0.5 and 1.0). Indeed, a power law relationship provides better fits for both samples with

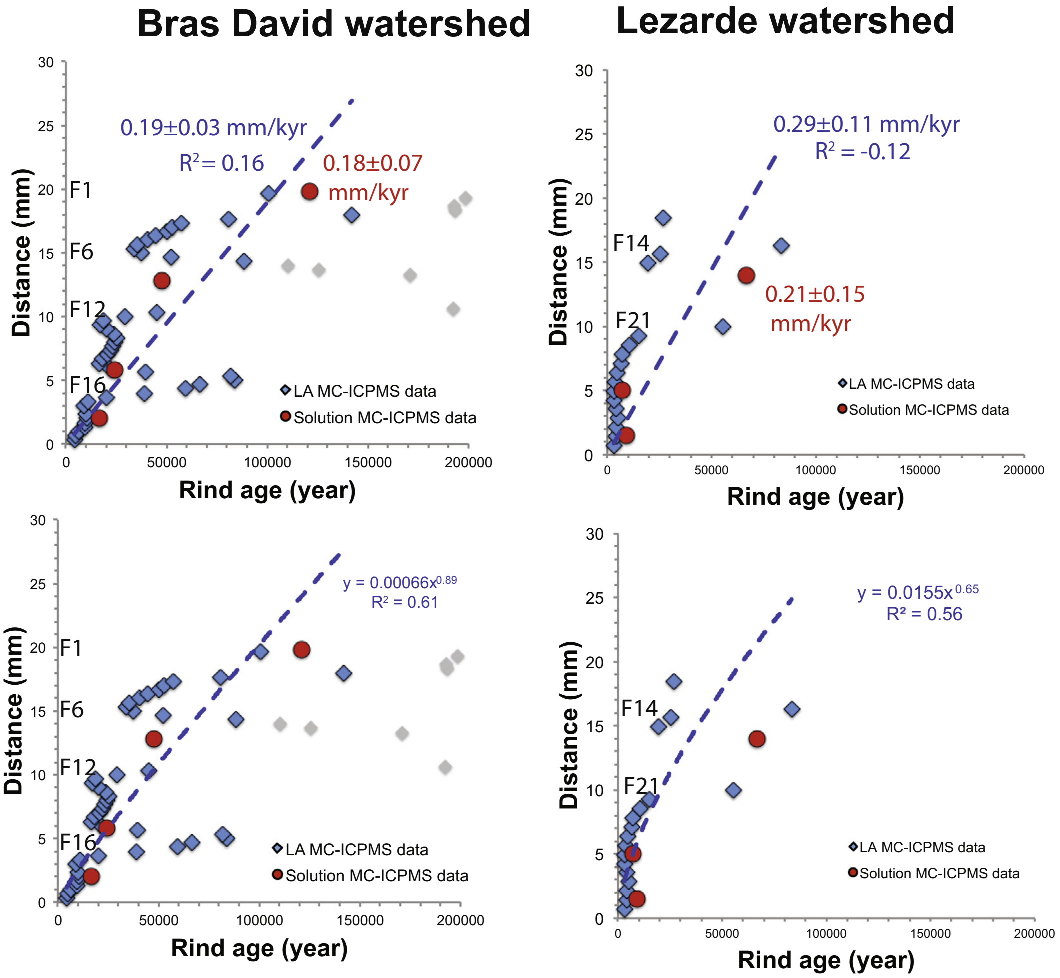

Fig. 8. Rind formation age as a function of the position relative to the core–rind boundary for clast BD (Bras David) and AN-14-3.2 (Lezarde). Dashed lines represent linear and power law regressions for each transect. Grey diamonds show samples near fractures and were not included in the regressions (see text for details).

correlation coefficients (R^2) ranging from 0.5 to 0.6 (Fig. 8). The fitted values for s are 0.65–0.90, consistent with the numerical model predictions (Lebedeva et al., 2015; Hunt, 2015). Such a power law relationship implies that as the observed thickness of the weathering rind increases, the weathering rate decreases, due to the consumption of available reactive materials as well as the effect of long transport distance to the weathering front. Indeed, a power law relationship has been used to describe a large number of available weathering rind studies globally and yielded values for s consistent with our model predictions (Hunt, 2015). In addition, changes in porosity during the increase of rind thickness may be critical to the decrease of weathering rates: for example, there may be critical porosities that are attained and can change the relationship (Navarre-Sitchler et al. 2011). Hence, the high spatial resolution that we have now obtained for the age-distance relationship within the rind system may document information about how the weathering rates changed over time.

It is well known that the influx of precipitation is an important control on the chemistry of streams and rivers (e.g., Godsey et al., 2009; Maher, 2010; Eiriksdottir et al., 2013; Maher and Chamberlain, 2014). A number of studies on Basse-Terre Island have focused on using both short- and long-term weathering systems (rivers, soils, and weathering rinds) to quantify the control of chemical weathering rates (Sak et al., 2010, 2018; Gaillardet et al., 2011; Ma et al., 2012; Engel et al., 2016; Buss et al., 2010; Clergue et al., 2015; Dessert et al., 2015). At the weathering rind scale, Lebedeva et al. (2015) presented a numerical model to show that the rind formation rate is predicted to be a direct function of a term ($C_e - C_R$), the difference between the equilibrium concentration (C_e) of the reactive component (a constant for constant temperature systems) and the concentration of this component in the pore fluid at the outermost boundary of the weathering clast (C_R). Watersheds that weather at the same temperature but with higher precipitation (MAP) are expected to have more

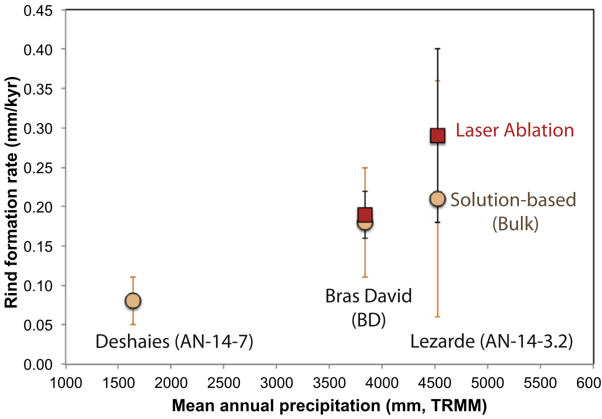

Fig. 9. Rind formation rates as a function of watershed precipitation (TRMM) on Basse-Terre Island. Rind formation rates were determined by LA MC-ICPMS (this study) and solution MC-ICPMS (Ma et al., 2012; Engel et al., 2016; Sak et al., 2018) for Deshaies, Brad David, and Lezarde watersheds; these watersheds show a similar linear relationship between riverine weathering fluxes and mean annual runoff (Gaillardet et al., 2011).

dilute soil pore water at any given depth and therefore higher values of ($C_e - C_R$). The Lebedeva et al. (2015) model is consistent with a linear increase in weathering rates with MAP during rind formation (Fig. 9). Notably, rind formation rates east of the topographic divide in the Lezarde watershed are the faster values (0.29 ± 0.11 mm/kyr by *in situ* measurements, or 0.21 ± 0.11 mm/kyr by bulk measurements despite of high uncertainties in rates), and the orographic precipitation patterns show a high MAP (~4500 mm; TRMM) for the windward part of the island. Along the precipitation gradient from the windward to the leeward, MAP values decrease to around 3500 mm in the Bras David watershed in the center and further to ~1800 mm in the Deshaies watershed in the northern island (Fig. 1). Rind formations rates also decrease to 0.19 ± 0.03 mm/kyr by *in situ* measurements (0.18 ± 0.07 mm/kyr by bulk measurements) in the Bras David watershed and to 0.08 ± 0.03 mm (by bulk measurements) in the Deshaies watershed (Engel et al., 2016). Such a comparison highlights a measurable effect of precipitation on chemical weathering over long time scales (e.g., over the formation duration of the rinds, ~70–100 kyr; Engel et al., 2016).

Furthermore, the current study shows that the rind ages could be determined with high spatial resolution by the LA U-series technique over the duration of formation of the rinds (e.g., at ~100 kyr). This highlights the potential use of this technique for reconstructions of paleo-weathering conditions in soil zones if such information (e.g. soil water chemistry or isotope ratios) is preserved in the rind record. Indeed, Pelt et al. (2008) have measured Sr isotope ratios in one Costa Rica clast and inferred variations in Sr isotope ratios in infiltrating soil water in the past. The combination of LA U-series technique with other isotope or elemental proxies from weathering rinds has potential to highlight changing weathering conditions in the past.

5. CONCLUSIONS

To explore the possibility of dating chemical weathering processes directly with in situ measurements of U-series disequilibria, we characterized two weathering rinds collected from Basse-Terre Island for U-series isotope compositions and elemental distributions with LA MC-ICPMS and LA Q-ICP MS. The in situ measurements of U-series disequilibria are consistent with the previous bulk measurements obtained from drilled bulk samples and conventional solution MC-ICPMS, but with much faster sample throughputs and a larger number of measurements with higher spatial resolution, despite larger analytical uncertainties. The rind formation age, rates, and parameters for U-series mobility modeled in this study are comparable to previous studies, and also reveal new insights into rind formation: the impact of micro-fractures on U-series mobility as well as the comparison of linear vs. power law rind thickness-age relationships, which were uncharacterizable by conventional solution-based MC-ICPMS measurements. In situ measurements in these weathering rinds also provide a valuable means to study the initiation and duration of chemical weathering in field systems, due to the presence of an easily identified core-rind boundary and the apparent absence of physical erosion during rind formation in regolith. We used LA-Q-ICPMS to map major and trace element distribution and to characterize the rind formation processes, such as dissolution, formation of new phases, development of porosity, and mobility behavior of elements at the weathering interfaces of clasts.

Our study highlights the potential of using in situ measurements of U-series disequilibria by LA-MC-ICPMS to quantifying weathering rates, with considerable analytical advantages compared to the solution MC-ICPMS method. More importantly, this study demonstrates a new way to determine weathering rates rapidly and accurately in a large number of rinds collected from multiple watersheds on Basse-Terre, which further allows us to quantify rind formation rates as a function of environmental variables such as climate at a watershed scale. In situ measurements in these weathering rinds also provide valuable means to study the initiation of chemical weathering in field systems as well as to infer weathering conditions in soil zones in the past.

ACKNOWLEDGEMENTS

This research was funded by the National Science Foundation grants EAR1251952 to LM, EAR1251969 to PBS, and EAR1251875 to SLB, and. We thank Celine Dessert (IPGP) and L'Observatoire Volcanologique et Sismologique de Guadeloupe (IPGP) for providing logistical support. LM also acknowledged Dr. Mark Engle (USGS) for support on statistical analysis.

APPENDIX A

See Tables A1 and A2.

Table A1
Laser ablation results for standard reference materials.

Reference Material	(234U/238U)	2SE	(230Th/238U)	2SE	(230Th/232Th)	2SE
NIST SRM 612						
G_NIST612_1_0	0.1806	0.0021	0.0690	0.0029	0.2171	0.0065
G_NIST612_1_1	0.1817	0.0020	0.0700	0.0027	0.2167	0.0077
G_NIST612_1_2	0.1829	0.0019	0.0689	0.0026	0.2071	0.0073
G_NIST612_1_4	0.1803	0.0023	0.0632	0.0023	0.1951	0.0067
G_NIST612_1_5	0.1785	0.0019	0.0630	0.0024	0.1993	0.0071
G_NIST612_2_0	0.1756	0.0018	0.0630	0.0023	0.1933	0.0065
G_NIST612_2_1	0.1762	0.0015	0.0637	0.0021	0.1866	0.0060
G_NIST612_2_2	0.1736	0.0018	0.0618	0.0019	0.1882	0.0057
G_NIST612_2_3	0.1745	0.0018	0.0536	0.0019	0.1692	0.0053
G_NIST612_2_4	0.1752	0.0015	0.0550	0.0020	0.1777	0.0063
G_NIST612_2_5	0.1731	0.0013	0.0554	0.0019	0.1713	0.0053
G_NIST612_2_6	0.1757	0.0021	0.0558	0.0020	0.1687	0.0057
G_NIST612_2_7	0.1747	0.0018	0.0568	0.0023	0.1715	0.0069
G_NIST612_2_8	0.1786	0.0040	0.0544	0.0018	0.1650	0.0053
G_NIST612_2_9	0.1741	0.0014	0.0600	0.0019	0.1759	0.0055
G_NIST612_2_10	0.1758	0.0022	0.0577	0.0051	0.1730	0.0160
G_NIST612_2_11	0.1743	0.0022	0.0584	0.0017	0.1746	0.0051
G_NIST612_2_12	0.1739	0.0020	0.0570	0.0020	0.1710	0.0063
G_NIST612_2_13	0.1746	0.0016	0.0552	0.0025	0.1734	0.0043
G_NIST612_2_14	0.1729	0.0016	0.0524	0.0030	0.1689	0.0071
G_NIST612_2_15	0.1744	0.0018	0.0563	0.0017	0.1716	0.0053
G_NIST612_2_16	0.1742	0.0016	0.0571	0.0018	0.1724	0.0053
G_NIST612_2_17	0.1749	0.0022	0.0564	0.0039	0.1700	0.0120
Average (this study)	**0.176**	**0.001**	**0.059**	**0.002**	**0.182**	**0.007**
Reference value (LA)[a]	**0.166**	**0.021**				
Reference value (MC ICP MS)[b]	**0.1725**	**0.0002**				
USGS BCR-2G						
G_BCR2G_1_0	1.0150	0.0310	1.0290	0.0460	0.8950	0.0400
G_BCR2G_1_1	0.9940	0.0280	1.0270	0.0580	0.9100	0.0450
G_BCR2G_1_2	1.0160	0.0240	1.0090	0.0550	0.8910	0.0480
G_BCR2G_1_5	0.9840	0.0210	0.9900	0.0360	0.8780	0.0320
G_BCR2G_1_6	0.9880	0.0230	0.9410	0.0420	0.8460	0.0350
G_BCR2G_1_7	1.0020	0.0190	0.9790	0.0460	0.8720	0.0430
G_BCR2G_2_0	1.0480	0.0210	1.1090	0.0350	0.9500	0.0300
G_BCR2G_2_1	1.0390	0.0210	1.0530	0.0380	0.9240	0.0330
G_BCR2G_2_2	1.0150	0.0200	1.0380	0.0420	0.9120	0.0380
G_BCR2G_2_3	0.9910	0.0220	1.0770	0.0630	0.9410	0.0620
G_BCR2G_2_4	1.0000	0.0230	0.9990	0.0450	0.8890	0.0400
G_BCR2G_2_5	1.0020	0.0220	0.9820	0.0390	0.8720	0.0340
G_BCR2G_2_6	0.9770	0.0210	1.0120	0.0480	0.8950	0.0420
G_BCR2G_2_7	1.0080	0.0270	0.9860	0.0710	0.8840	0.0620
G_BCR2G_2_8	1.0030	0.0220	0.9480	0.0380	0.8380	0.0330
G_BCR2G_2_9	0.9950	0.0230	1.0140	0.0800	0.9260	0.0890
G_BCR2G_2_10	1.0030	0.0620	0.9300	0.0360	0.8240	0.0310
G_BCR2G_2_11	0.9680	0.0240	0.9500	0.0470	0.8470	0.0420
G_BCR2G_2_12	0.9950	0.0270	0.9680	0.0520	0.8350	0.0440
G_BCR2G_2_13	0.9920	0.0200	0.9590	0.0450	0.8630	0.0430
G_BCR2G_2_14	0.9650	0.0250	0.9160	0.0510	0.8290	0.0450
Average (this study)	**1.000**	**0.004**	**0.996**	**0.005**	**0.882**	**0.006**
Reference value (LA)[a]	**0.994**	**0.014**	**1.000**	**0.006**	**0.873**	**0.015**
Reference value (TIMS)[c]	**1.001**	**0.003**	**0.990**	**0.008**	**0.877**	**0.006**
USGS BHVO-2G						
G_BHVO2G_1_0	0.9990	0.0470	1.0530	0.0890	1.1040	0.0940
G_BHVO2G_1_1	0.9650	0.0370	1.1700	0.1000	1.2300	0.1100
G_BHVO2G_1_2	0.9690	0.0390	1.0690	0.0900	1.1280	0.0980
G_BHVO2G_1_3	1.0100	0.0510	1.0100	0.1100	1.0700	0.1100
G_BHVO2G_1_4	0.9690	0.0500	0.9300	0.0930	1.0000	0.1000

(*continued on next page*)

Table A1 (*continued*)

Reference Material	(234U/238U)	2SE	(230Th/238U)	2SE	(230Th/232Th)	2SE
G_BHVO2G_1_5	1.0030	0.0550	1.0300	0.1100	1.1200	0.1200
G_BHVO2G_2_0	1.0080	0.0540	1.0240	0.0740	1.0630	0.0740
G_BHVO2G_2_1	1.0100	0.0440	1.2300	0.1000	1.3100	0.1100
G_BHVO2G_2_2	1.0060	0.0640	1.0800	0.1200	1.1300	0.1300
G_BHVO2G_2_3	0.9980	0.0410	1.0800	0.1000	1.1700	0.1100
G_BHVO2G_2_4	0.9940	0.0510	1.0220	0.0990	1.1000	0.1000
G_BHVO2G_2_5	0.9620	0.0450	1.0360	0.0960	1.1000	0.1000
G_BHVO2G_2_6	0.9590	0.0480	1.0140	0.0900	1.0670	0.0950
G_BHVO2G_2_7	0.9720	0.0470	1.0010	0.0980	1.0500	0.1000
G_BHVO2G_2_8	0.9840	0.0450	0.9310	0.0910	1.0020	0.0950
G_BHVO2G_2_9	0.9760	0.0440	1.0050	0.0610	1.1010	0.0650
G_BHVO2G_2_10	0.9620	0.0440	0.9420	0.0960	1.0200	0.1000
G_BHVO2G_2_11	0.9600	0.0530	0.9830	0.0870	1.0360	0.0910
G_BHVO2G_2_12	1.0000	0.0480	1.0800	0.1100	1.1400	0.1200
G_BHVO2G_2_13	0.9700	0.0390	0.9600	0.1200	1.0100	0.1200
G_BHVO2G_2_14	0.9780	0.0460	0.9810	0.0930	1.0500	0.1000
G_BHVO2G_2_15	1.0350	0.0500	0.9410	0.0860	1.0630	0.0910
G_BHVO2G_2_16	1.0380	0.0390	0.9200	0.1000	1.0100	0.1100
G_BHVO2G_2_17	1.0050	0.0610	0.9300	0.1200	1.0200	0.1300
Average (this study)	**0.989**	**0.003**	**1.018**	**0.006**	**1.087**	**0.006**
Reference value (LA)[a]	**0.988**	**0.029**	**1.006**	**0.035**	**1.078**	**0.032**
Reference value (TIMS)[c]	**1.000**	**0.002**	**1.002**	**0.007**	**1.090**	**0.007**

[a] Mertz-Kraus et al. (2010).

[b] Stirling et al. (2000).

[c] Matthews et al. (2008).

Table A2

Laser ablation results for weathering clast samples.

Sample	LA subsample	Step ID	Material	(234U/238U)	2SE	(230Th/238U)	2SE	(230Th/232Th)	2SE	(238U/232Th)	2SE
Bras David	BRAS_DAVID_0	1	core	0.964	0.062	1.025	0.090	1.000	0.100	0.976	0.130
	BRAS_DAVID_1	2	core	1.017	0.045	1.053	0.073	1.066	0.074	1.012	0.099
	BRAS_DAVID_2	3	core	0.965	0.055						
	BRAS_DAVID_3	4	core	0.950	0.079						
	BRAS_DAVID_4	5	core	1.121	0.152						
	BRAS_DAVID_5	6	core	1.049	0.082	1.040	0.170	0.890	0.130	0.856	0.188
	BRAS_DAVID_6	7	core	1.192	0.333						
	BRAS_DAVID_7	8	core	0.929	0.131						
	BRAS_DAVID_8	9	core	1.081	0.101	1.320	0.380	1.730	0.930	1.311	0.799
	BRAS_DAVID_9	10	core	0.909	0.077						
	BRAS_DAVID_10	11	core	1.121	0.111						
	BRAS_DAVID_11	12	core	0.995	0.062						
	BRAS_DAVID_12	13	core	0.920	0.058						
	BRAS_DAVID_13	14	core	0.935	0.047	0.956	0.097	0.930	0.100	0.973	0.144
	BRAS_DAVID_14	15	core	1.041	0.101						
	BRAS_DAVID_15	16	core	0.986	0.046	1.012	0.076	0.967	0.074	0.956	0.102
	BRAS_DAVID_16	17	core	1.000	0.061						
	BRAS_DAVID_17	18	core	0.919	0.111						
	BRAS_DAVID_18	19	core	1.008	0.072						
	BRAS_DAVID_19	20	core	0.952	0.063	1.030	0.100	0.952	0.090	0.924	0.125
	BRAS_DAVID_20	21	core	0.973	0.047	1.002	0.087	0.957	0.086	0.955	0.119
	BRAS_DAVID_21	22	core	1.041	0.273						
	BRAS_DAVID_22	23	core	1.051	0.111						
	BRAS_DAVID_23	24	core	1.020	0.121						
	BRAS_DAVID_24	25	core	0.980	0.111						
	BRAS_DAVID_25	26	core	0.923	0.056	0.933	0.062	0.977	0.079	1.047	0.110
	BRAS_DAVID_26	27	core	1.039	0.047	0.990	0.120	0.960	0.110	0.970	0.162
	BRAS_DAVID_27	28	core	0.951	0.043	0.970	0.120	0.970	0.120	1.000	0.175

(*continued on next page*)

Table A2 (*continued*)

Sample	LA subsample	Step ID	Material	(234U/ 238U)	2SE	(230Th/ 238U)	2SE	(230Th/ 232Th)	2SE	(238U/ 232Th)	2SE
	BRAS_DAVID_28	29	core	0.981	0.062						
	BRAS_DAVID_29	30	core	0.935	0.051	1.030	0.100	1.060	0.110	1.029	0.146
	BRAS_DAVID_30	31	core	0.963	0.057	0.899	0.073	0.875	0.090	0.973	0.128
	BRAS_DAVID_31	32	core	0.936	0.046	0.987	0.093	1.010	0.170	1.023	0.197
	BRAS_DAVID_32	33	core	0.964	0.043	0.968	0.077	1.002	0.086	1.035	0.121
	BRAS_DAVID_33	34	core	0.966	0.060	0.930	0.100	1.020	0.110	1.097	0.167
	BRAS_DAVID_34	35	core	1.004	0.050	1.050	0.110	1.050	0.110	1.000	0.148
	BRAS_DAVID_35	36	core	0.954	0.048	0.990	0.083	1.000	0.085	1.010	0.121
	BRAS_DAVID_36	37	core	0.974	0.060						
	BRAS_DAVID_37	38	core	0.953	0.050	0.991	0.097	0.992	0.096	1.001	0.138
	BRAS_DAVID_38	39	core	0.917	0.041	0.947	0.080	0.954	0.078	1.007	0.118
	BRAS_DAVID_39	40	core	0.937	0.086	1.040	0.140	1.090	0.150	1.048	0.202
	BRAS_DAVID_40	41	core	0.975	0.069						
	BRAS_DAVID_41	42	core	0.947	0.045	1.024	0.092	0.988	0.088	0.965	0.122
	BRAS_DAVID_42	43	core	0.953	0.057	0.990	0.110	0.937	0.094	0.946	0.142
	BRAS_DAVID_43	44	core	0.978	0.042	0.980	0.110	0.940	0.100	0.959	0.148
	BRAS_DAVID_44	45	core	0.940	0.043	0.943	0.086	0.955	0.094	1.013	0.136
	BRAS_DAVID_45	46	core	0.908	0.056						
	BRAS_DAVID_46	47	core	0.940	0.052	1.050	0.100	1.050	0.100	1.000	0.135
	BRAS_DAVID_47	48	core	0.936	0.057	0.870	0.110	0.900	0.120	1.034	0.190
	BRAS_DAVID_48	49	core	0.972	0.052						
	BRAS_DAVID_49	50	core	0.920	0.062						
	BRAS_DAVID_50	51	core	0.968	0.055	0.905	0.098	0.907	0.092	1.002	0.149
	BRAS_DAVID_51	52	rind	0.919	0.026	0.826	0.045	0.845	0.046	1.023	0.079
	BRAS_DAVID_52	53	rind	0.950	0.045	0.620	0.063	0.806	0.069	1.300	0.173
	BRAS_DAVID_53	54	rind	0.914	0.040	0.696	0.063	0.893	0.080	1.283	0.163
	BRAS_DAVID_54	55	rind	0.945	0.062	0.610	0.100	0.812	0.093	1.331	0.266
	BRAS_DAVID_55	56	rind	0.928	0.041	0.780	0.073	0.847	0.075	1.086	0.140
	BRAS_DAVID_56	57	rind	0.954	0.044	0.643	0.065	0.826	0.064	1.285	0.164
	BRAS_DAVID_57	58	rind	0.957	0.039	0.870	0.190	1.100	0.270	1.264	0.415
	BRAS_DAVID_58	59	rind	1.111	0.222						
	BRAS_DAVID_59	60	rind	0.901	0.036	0.733	0.078	0.920	0.120	1.255	0.211
	BRAS_DAVID_60	61	rind	0.931	0.036	0.723	0.063	0.899	0.083	1.243	0.158
	BRAS_DAVID_61	62	rind	0.921	0.032	0.741	0.078	0.839	0.080	1.132	0.161
	BRAS_DAVID_62	63	rind	0.970	0.048	0.611	0.085	0.840	0.110	1.375	0.263
	BRAS_DAVID_63	64	rind	0.984	0.042	0.601	0.079	0.910	0.110	1.514	0.270
	BRAS_DAVID_64	65	rind	0.980	0.121						
	BRAS_DAVID_65	66	rind	0.924	0.058						
	BRAS_DAVID_66	67	rind	0.964	0.045	0.760	0.170	1.010	0.230	1.329	0.424
	BRAS_DAVID_67	68	rind	0.937	0.048	0.720	0.110	0.880	0.120	1.222	0.250
	BRAS_DAVID_68	69	rind	0.979	0.039	0.590	0.084	0.920	0.120	1.559	0.301
	BRAS_DAVID_69	70	rind	0.926	0.037	0.686	0.057	0.857	0.075	1.249	0.151
	BRAS_DAVID_70	71	rind	0.935	0.037	0.627	0.039	0.882	0.064	1.407	0.134
	BRAS_DAVID_71	72	rind	0.923	0.033	0.710	0.087	0.900	0.120	1.268	0.230
	BRAS_DAVID_72	73	rind	0.936	0.037	0.730	0.110	0.960	0.220	1.315	0.361
	BRAS_DAVID_73	74	rind	0.924	0.047						
	BRAS_DAVID_74	75	rind	0.953	0.044	0.610	0.066	0.970	0.110	1.590	0.249
	BRAS_DAVID_75	76	rind	0.923	0.032	0.700	0.150	0.980	0.280	1.400	0.500
	BRAS_DAVID_76	77	rind	0.968	0.048	0.628	0.082	0.890	0.110	1.417	0.255
	BRAS_DAVID_77	78	rind	0.911	0.036	0.660	0.069	0.915	0.089	1.386	0.198
	BRAS_DAVID_78	79	rind	0.927	0.035	0.660	0.110	0.930	0.160	1.409	0.338
	BRAS_DAVID_79	80	rind	0.944	0.029	0.657	0.076	0.841	0.097	1.280	0.209
	BRAS_DAVID_80	81	rind	0.928	0.033	0.600	0.057	0.808	0.077	1.347	0.181
	BRAS_DAVID_81	82	rind	0.916	0.037	0.606	0.047	0.799	0.069	1.318	0.153
	BRAS_DAVID_82	83	rind	0.950	0.035	0.670	0.180	1.180	0.340	1.761	0.694
	BRAS_DAVID_83	84	rind	1.030	0.162						
	BRAS_DAVID_84	85	rind	0.972	0.044						
	BRAS_DAVID_85	86	rind	0.980	0.162						
	BRAS_DAVID_86	87	rind	0.937	0.051	0.542	0.066	1.070	0.160	1.974	0.381
	BRAS_DAVID_87	88	rind	0.948	0.073						
	BRAS_DAVID_88	89	rind	0.995	0.041						

(*continued on next page*)

Table A2 (*continued*)

Sample	LA subsample	Step ID	Material	(234U/ 238U)	2SE	(230Th/ 238U)	2SE	(230Th/ 232Th)	2SE	(238U/ 232Th)	2SE
	BRAS_DAVID_89	90	rind	0.963	0.050						
	BRAS_DAVID_90	91	rind	1.054	0.066						
	BRAS_DAVID_91	92	rind	0.948	0.053						
	BRAS_DAVID_92	93	rind	0.929	0.073						
	BRAS_DAVID_93	94	rind	0.924	0.029	0.635	0.043	0.866	0.061	1.364	0.133
	BRAS_DAVID_94	95	rind	0.938	0.025	0.615	0.043	0.926	0.058	1.506	0.141
	BRAS_DAVID_95	96	rind	0.933	0.039	0.630	0.210	0.934	0.088	1.483	0.514
	BRAS_DAVID_96	97	rind	0.981	0.034	0.577	0.052	0.868	0.076	1.504	0.189
	BRAS_DAVID_97	98	rind	0.936	0.034	0.552	0.062	0.950	0.110	1.721	0.278
	BRAS_DAVID_98	99	rind	0.910	0.026	0.547	0.042	0.894	0.078	1.634	0.190
	BRAS_DAVID_99	100	rind	0.946	0.025	0.576	0.040	0.892	0.056	1.549	0.145
	BRAS_DAVID_100	101	rind	0.931	0.023	0.540	0.040	0.850	0.063	1.574	0.165
	BRAS_DAVID_101	102	rind	0.933	0.023	0.580	0.130	1.030	0.250	1.776	0.587
	BRAS_DAVID_102	103	rind	0.932	0.022	0.575	0.061	0.990	0.100	1.722	0.252
	BRAS_DAVID_103	104	rind	0.950	0.062						
	BRAS_DAVID_104	105	rind	0.960	0.057	0.640	0.130	1.030	0.210	1.609	0.463
	BRAS_DAVID_105	106	rind	0.912	0.024	0.585	0.044	1.045	0.082	1.786	0.194
	BRAS_DAVID_106	107	rind	0.925	0.032	0.572	0.039	1.240	0.130	2.168	0.271
	BRAS_DAVID_107	108	rind	0.923	0.033						
	BRAS_DAVID_108	109	rind	0.953	0.044	0.637	0.094	1.060	0.140	1.664	0.330
	BRAS_DAVID_109	110	rind	0.982	0.090						
	BRAS_DAVID_109	111	rind	0.984	0.090						
	BRAS_DAVID_108	112	rind	1.028	0.047	0.690	0.100	0.647	0.085	0.938	0.183
	BRAS_DAVID_109	113	rind	1.060	0.097						

Sample	LA subsample	Step ID	Material	(234U/ 238U)	2SE	(230Th/ 238U)	2SE	(230Th/ 232Th)	2SE	(238U/ 232Th)	2SE
AN-14-3.2	AN-14-3.2	1	Core	1.005	0.057	1.090	0.130	0.840	0.130	0.771	0.151
	AN-14-3.2 LINE #5	2	Core	1.031	0.042	0.980	0.110	0.920	0.110	0.939	0.154
	AN-14-3.2 LINE #6	3	Core	1.016	0.056	1.000	0.130	0.910	0.110	0.910	0.162
	AN-14-3.2 LINE #7	4	Core	1.032	0.050	0.968	0.094	1.000	0.110	1.033	0.152
	AN-14-3.2 LINE #8	5	Core	0.992	0.044	0.966	0.071	0.982	0.072	1.017	0.106
	AN-14-3.2 LINE #9	6	Core	0.959	0.049	0.950	0.140	1.030	0.150	1.084	0.225
	AN-14-3.2 LINE #10	7	Core	0.917	0.034	0.987	0.054	1.017	0.057	1.030	0.081
	AN-14-3.2 LINE #11	8	Core	1.008	0.055	1.040	0.110	1.030	0.120	0.990	0.156
	AN-14-3.2 LINE #12	9	Core	0.959	0.032	0.955	0.086	1.047	0.090	1.096	0.136
	AN-14-3.2 LINE #13	10	rind	0.937	0.032	0.708	0.078	1.081	0.084	1.527	0.206
	AN-14-3.2 LINE #14	11	rind	0.965	0.027	0.785	0.050	1.002	0.081	1.276	0.131
	AN-14-3.2 LINE #15	12	rind	0.910	0.031	0.789	0.053	0.992	0.058	1.257	0.112
	AN-14-3.2 LINE #16	13	rind	0.988	0.027	0.835	0.048	0.879	0.056	1.053	0.090
	AN-14-3.2 LINE #17	14	rind	0.998	0.030	0.844	0.051	0.952	0.058	1.128	0.097
	AN-14-3.2 LINE #18	15	rind	1.006	0.028	0.802	0.062	0.957	0.078	1.193	0.134
	AN-14-3.2 LINE #19	16	rind	1.008	0.042	0.842	0.078	1.003	0.080	1.191	0.146
	AN-14-3.2 LINE #20	17	rind	1.008	0.031	0.736	0.063	0.951	0.081	1.292	0.156
	AN-14-3.2 LINE #21	18	rind	0.988	0.025	0.813	0.050	0.979	0.055	1.204	0.100
	AN-14-3.2 LINE #22	19	rind	1.013	0.023	0.710	0.044	0.877	0.052	1.235	0.106
	AN-14-3.2 LINE #23	20	rind	1.012	0.032	0.692	0.049	0.949	0.055	1.371	0.125
	AN-14-3.2 LINE #24	21	rind	1.018	0.038	0.757	0.060	0.954	0.061	1.260	0.128
	AN-14-3.2 LINE #25	22	rind	0.964	0.049	0.712	0.064	0.989	0.088	1.389	0.176
	AN-14-3.2 LINE #26	23	rind	0.981	0.041	0.679	0.042	1.098	0.084	1.617	0.159
	AN-14-3.2 LINE #27	24	rind	1.002	0.027	0.712	0.068	1.110	0.150	1.559	0.258
	AN-14-3.2 LINE #28	25	rind	1.065	0.025						
	AN-14-3.2 LINE #29	26	rind	1.004	0.025	0.762	0.049	1.043	0.063	1.369	0.121
	AN-14-3.2 LINE #30	27	rind	0.979	0.023	0.779	0.066	1.111	0.078	1.426	0.157
	AN-14-3.2 LINE #31	28	rind	1.001	0.026	0.723	0.046	1.089	0.084	1.506	0.151
	AN-14-3.2 LINE #32	29	rind	1.030	0.045						
	AN-14-3.2 LINE #33	30	rind	1.040	0.038	0.757	0.039	1.220	0.072	1.612	0.126
	AN-14-3.2 LINE #34	31	rind	0.991	0.035	0.747	0.058	1.048	0.072	1.403	0.145
	AN-14-3.2 LINE #35	32	rind	1.000	0.040	0.792	0.053	1.078	0.068	1.361	0.125
	AN-14-3.2 LINE #36	33	rind	1.017	0.036	0.904	0.071	1.740	0.240	1.925	0.306
	AN-14-3.2 LINE #37	34	rind	0.999	0.054						

(*continued on next page*)

Table A2 (*continued*)

Sample	LA subsample	Step ID	Material	(234U/ 238U)	2SE	(230Th/ 238U)	2SE	(230Th/ 232Th)	2SE	(238U/ 232Th)	2SE
	AN-14-3.2 LINE #38	35	crust	0.932	0.290	0.360	0.610	0.800	1.400	2.222	5.413
	AN-14-3.2 LINE #39	36	crust	0.932	0.040	1.120	0.110	1.080	0.110	0.964	0.136
	AN-14-3.2 LINE #40	37	crust	1.001	0.064	1.080	0.120	1.150	0.120	1.065	0.162
	AN-14-3.2 LINE #41	38	soil	1.021	0.075	1.530	0.330	1.430	0.230	0.935	0.251
	AN-14-3.2 LINE #42	39	soil	0.776	0.066	0.940	0.200	1.320	0.350	1.404	0.477
	AN-14-3.2 LINE #43	40	soil	0.939	0.068	1.170	0.110	1.210	0.120	1.034	0.141
	AN-14-3.2 LINE #44	41	soil	0.932	0.207	1.600	0.680	2.500	1.200	1.563	1.002
	AN-14-3.2 LINE #45	42	soil	0.943	0.085	1.420	0.160	1.480	0.150	1.042	0.158
	AN-14-3.2 LINE #46	43	soil	1.079	0.076	1.170	0.220	2.160	0.450	1.846	0.518
	AN-14-3.2 LINE #47	44	soil	0.977	0.092	0.860	0.190	3.180	0.630	3.698	1.097
	AN-14-3.2 LINE #48	45	soil	0.944	0.066	0.772	0.099	3.160	0.400	4.093	0.738
	AN-14-3.2 LINE #49	46	soil	1.051	0.092	1.660	0.390	4.100	1.000	2.470	0.836
	AN-14-3.2 LINE #50	47	soil	1.388	0.218	2.750	0.870	3.900	1.300	1.418	0.652
	AN-14-3.2 LINE #51	48	soil	1.045	0.064	1.720	0.310	1.600	0.290	0.930	0.238
	AN-14-3.2 LINE #52	49	soil	1.060	0.095	1.530	0.210	1.200	0.160	0.784	0.150
	AN-14-3.2 LINE #53	50	soil	0.950	0.074	1.270	0.150	1.020	0.130	0.803	0.140

APPENDIX B. SUPPLEMENTARY MATERIAL

Supplementary data to this article can be found online at https://doi.org/10.1016/j.gca.2018.12.020.

REFERENCES

Ames L. L., McGarrah J. E. and Walker B. A. (1983) Sorption of trace constituents from aqueous solutions onto secondary minerals. I. Uranium. *Clay Clay Mineral.* **31**, 321–334.

Andersen M. B., Erel Y. and Bourdon B. (2009) Experimental evidence for 234U–238U fractionation during granite weathering with implications for 234U/238U in natural waters. *Geochim. Cosmochim. Acta* **73**, 4124–4141.

Anderson S. P., Dietrich W. E. and Brimhall G. H. (2002) Weathering profiles, mass-balance analysis, and rates of solute loss: linkage between weathering and erosion in a small, steep catchment. *Geol. Soc. Am. Bull.* **114**, 1143–1158.

Andersson P. S., Porcelli D., Wasserburg G. J. and Ingri J. (1998) Particle transport of 234U–238U in the Kalix River and in the Baltic Sea. *Geochim. Cosmochim. Acta* **62**, 385–392.

Bernal J., Eggins S. and McCulloch M., et al. (2006) Dating of chemical weathering processes by in situ measurement of U-series disequilibria in supergene Fe-oxy/hydroxides using LA-MC-ICPMS. *Chem. Geol.* **235**(1–2), 76–94.

Berner R. A., Lasaga A. and Garrels R. M. (1983) The carbonate-silicate geochemical cycle and its effect on atmospheric carbon dioxide over the past 100 million years. *Am. J. Sci.* **283**, 641–683.

Bourdon B., Bureau S., Andersen M. B., Pili E. and Hubert A. (2009) Weathering rates from top to bottom in a carbonate environment. *Chem. Geol.* **258**, 275–287.

Bourdon B., Henderson G. M., Lundstrom C. C. and Turner S. P. (2003) Uranium-series geochemistry. *Mineralog. Soc. Am. Rev. Mineral. Geochem.* **52**, 656.

Buss H. L., Sak P. B., Webb S. M. and Brantley S. L. (2008) Weathering of the Rio Blanco quartz diorite, Luquillo Mountains, Puerto Rico: coupling oxidation, dissolution, and fracturing. *Geochim. Cosmochim. Acta* **72**, 4488–4507.

Buss H. L., White A. F., Dessert C., Gaillardet J., Blum A. E. and Sak P. B. (2010) Depth profiles in a tropical, volcanic critical zone observatory: Basse-Terre, Guadeloupe. *Torres-Alvarado, I.S.*.

Chabaux F., Bourdon B. and Riotte J. (2008) U-series geochemistry in weathering profiles, river waters and lakes. *Radioact. Environ.* **13**, 49–104.

Chabaux F., Riotte J. and Dequincey O. (2003) U-Th-Ra fractionation during weathering and river transport. *Rev. Mineral. Geochem.* **52**, 533–576.

Chadwick O. A., Derry L. A., Vitousek P. M., Huebert B. J. and Hedin L. O. (1999) Changing sources of nutrients during four million years of ecosystem development. *Nature* **397**, 491–497.

Clergue C. et al. (2015) Influence of atmospheric deposits and secondary minerals on Li isotopes budget in a highly weathered catchment, Guadeloupe (Lesser Antilles). *Chem. Geol.* **414**, 28–41. https://doi.org/10.1016/j.chemgeo.2015.08.015.

Condomines M., Gauthier P.-J. and Sigmarsson O. (2003) Timescales of magma chamber processes and dating of young volcanic rocks. *Rev. Mineral. Geochem.* **52**, 125–174.

DePaolo D. J., Maher K., Christensen J. N. and McManus J. (2006) Sediment transport time measured with U-series isotopes: results from ODP North Atlantic drift site 984. *Earth Planet. Sci. Lett.* **248**, 394–410.

Dequincey O., Chabaux F., Clauer N., Sigmarsson O., Liewig N. and Leprun J.-C. (2002) Chemical mobilizations in laterites: evidence from trace elements and 238U–234U-230Th disequilibria. *Geochim. Cosmochim. Acta* **66**, 1197–1210.

Derry L. A., Kurtz A. C., Ziegler K. and Chadwick O. A. (2005) Biological control of terrestrial silica cycling and export fluxes to watersheds. *Nature* **433**, 728–731.

Dessert C., Lajeunesse E., Lloret E., Clergue C., Crispi O., Gorge C. and Quidelleur X. (2015) Controls on chemical weathering on a mountainous volcanic tropical island: Guadeloupe (French West Indies). *Geochim. Cosmochim. Acta* **171**, 216–237.

Dosseto A., Bourdon B., Gaillardet J., Allegre C. J. and Filizola N. (2006) Timescale and conditions of chemical weathering under tropic climate: study of the Amazon basin with U-series.

Dosseto A. (2015) Chemical Weathering (U-Series). *Encycloped. Sci. Dat. Methods*, 152–169.

Dosseto A., Bourdon B. and Turner S. P. (2008a) Uranium-series isotopes in river materials: insights into the timescales of erosion and sediment transport. *Earth Planet. Sci. Lett.* **265**, 1–17.

Dosseto A., Turner S. P. and Chappell J. (2008b) The evolution of weathering profiles through time: new insights from uranium-series isotopes. *Earth Planet. Sci. Lett.* **274**, 359–371.

Drever, J.I., 2004. Surface and ground water, weathering, and soils. In Treatise on Geochemistry, Volume 5, Holland, H.D., and Turekian (Eds.), Elsevier, 626 pp.

Duff M. C., Coughlin J. U. and Hunter D. B. (2002) Uranium coprecipitation with iron oxide minerals. *Geochim. Cosmochim. Acta* **66**, 3533–3547.

Edwards R. L., Gallup C. D. and Cheng H. (2003) Uranium-series dating of marine and lacustrine carbonates. *Rev. Mineral. Geochem.* **52**, 363–405.

Eggins S., Grün R. and McCulloch M., et al. (2005) In situ U-series dating by laser-ablation multi-collector ICPMS: new prospects for Quaternary geochronology. *Quatern. Sci. Rev.* **24**(23–24), 2523–2538.

Eiriksdottir E. S., Gislason S. R. and Oelkers E. H. (2013) Does temperature or runoff control the feedback between chemical denudation and climate? Insights from NE Iceland. *Geochim. Cosmochim. Acta* **107**, 65–81.

Engel J., Ma L., Sak P., Gaillardet J., Ren M., Engle M. and Brantley S. (2016) Quantifying chemical weathering rates along a precipitation gradient on Basse-Terre Island, French Guadeloupe: new insights from U-series isotopes in weathering rinds. *Geochim. Cosmochim. Acta* **195**, 29–67.

Fleischer R. L. (1980) Isotopic disequilibrium of uranium: alpharecoil damage and preferential solution effects. *Science* **207**, 979–981.

Gaillardet J., Dupré B., Louvat P. and Allègre C. J. (1999) Global silicate weathering and CO_2 consumption rates deduced from the chemistry of large rivers. *Chem. Geol.* **159**, 3–30.

Gaillardet J., Rad S., Rive K., Louvat P., Gorge C., Allegre C. J. and Lajeunesse R. (2011) Orography-driven chemical denudation in the Lesser Antilles: evidence for a new feed-back mechanism stabilizing atmospheric CO_2. *Am. J. Sci.* **311**, 851–894.

Gascoyne M. (1992) Geochemistry of the actinides and their daughters. In *Uranium-Series Disequilibrium: Application to Earth, Marine, and Environmental Sciences* (eds. M. Ivanovich and R. S. Harmon). Oxford Sciences Publications, Oxford, pp. 34–61.

Ghaleb B., Hillaire-Marcel C., Causse C., Gariepy C. and Vallieres S. (1990) Fractionation and recycling of U and Th isotopes in a semiarid endoreic depression of central Syria. *Geochim. Cosmochim. Acta* **54**, 1025–1035.

Godsey S. E., Kirchner J. W. and Clow D. W. (2009) Concentration-discharge relationships reflect chemostatic characteristics of US catchments. *Hydrol. Proc.* **23**, 1844–1864.

Granet M., Chabaux F., Stille P., Dosseto A., France-Lanord C. and Blaes E. (2010) U-series disequilibria in suspended river sediments and implication for sediment transfer time in alluvial plains: the case of the Himalayan rivers. *Geochim. Cosmochim. Acta* **74**, 2851–2865.

Granet M., Chabaux F., Stille P., France-Lanord C. and Pelt E. (2007) Time-scales of sedimentary transfer and weathering processes from U-series nuclides: clues from the Himalayan Rivers. *Earth Planet. Sci. Lett.* **261**, 389–406.

Hawkesworth C. J. and Powell M. (1980) Magma genesis in the Lesser Antilles Island arc. *Earth Planet. Sci. Lett.* **51**, 297–308.

Hilley G. E. and Porder S. (2008) A framework for predicting global silicate weathering and CO_2 drawdown rates over geological time-scales. *PNAS* **105**, 16855–16859.

Hunt A. (2015) Predicting rates of weathering rind formation. *Vadose Zone J.*. https://doi.org/10.2136/vzj2014.09.0123.

Hunt Alle and Sahimi Muhamma (2017) Transport and reaction in porous media: percolation scaling, critical-path analysis, and effective-medium approximation. *Rev. Geophys.* **55**. https://doi.org/10.1002/2017RG000558.

Ivanovich M. and Harmon R. S. (1992) *Uranium-series Disequilibrium: Applications to Earth, Marine, and Environmental Sciences*. Clarendon Press, Oxford.

Jochum K. P., Willbold M., Raczek I., Stoll B. and Herwig K. (2005) Chemical characterisation of the USGS reference glasses GSA-1G, GSC-1G, GSD-1G, GSE-1G, BCR-2G, BHVO-2G and BIR-1G using EPMA, ID-TIMS, ID-ICP-MS and LA-ICP-MS. *Geostand. Geoanalyt. Res.* **29**, 285–302.

Jordan T. H. (1975) The present-day motion of the Caribbean plate. *J. Geophys. Res.* **80**, 4433–4439.

Krishnaswawi S., Williams G. A., Graustein W. C. and Turekian K. K. (2004) The effect of weathering regime on uranium decay series and osmium in two soil profiles. *Geochem. J.* **38**, 651–660.

Latham A. G. and Schwarcz H. P. (1987a) On the possibility of determining rates of removal of uranium from crystalline igneous rocks using U-series disequilibria – 1: a U-leach model, and its applicability to whole-rock data. *Appl. Geochem.* **2**, 55–65.

Latham A. G. and Schwarcz H. P. (1987b) On the possibility of determining rates of removal of uranium from crystalline igneous rocks using U-series disequilibria – 2: applicability of a U-leach model to mineral separates. *Appl. Geochem.* **2**, 67–71.

Lear J., Hare D., Adlard P., Finkelstein D. and Doble P. (2012) Improving acquisition times of elemental bio-imaging for quadrupole-based LA-ICP-MS. *J. Anal. At. Spectrom.* **27**, 159–164.

Lebedeva M. I., Sak P. B., Ma L. and Brantley S. L. (2015) Using a mathematical model of a weathering clast to explore the effects of curvature on weathering. *Chem. Geol.* **404**, 88–99.

Liu Y., Hu Z., Gao S., Günther D., Xu J., Gao C. and Chen H. (2008) In situ analysis of major and trace elements of anhydrous minerals by LA-ICP-MS without applying an internal standard. *Chem. Geol.* **257**, 34–43.

Lloret E., Dessert C., Gaillardet J., Alberic P., Crispi O., Chaduteau C. and Benedetti M. F. (2011) Comparison of dissolved inorganic and organic carbon export in the rivers of tropical volcanic island; example from Guadeloupe, French West Indies. *Chem. Geol.* **280**, 65–78.

Ma J.-L., Wei G.-J., Xu Y.-G., Long W.-G. and Sun W.-D. (2007) Mobilization and re-distribution of major and trace elements during extreme weathering of basalt in Hainan Island, South China. *Geochim. Cosmochim. Acta* **71**, 3223–3237.

Ma L. (2018) Major element concentrations in weathering rinds and andesitic cores of Basse-Terre Island (French Guadeloupe). *Earthchem. Library Database*. https://doi.org/10.1594/IEDA/111220.

Ma L., Chabaux F., Pelt E., Blaes E., Jin L. and Brantley S. L. (2010) Regolith production rates calculated with uranium-series isotopes at Susquehanna/Shale Hills Critical Zone Observatory. *Earth Planet. Sci. Lett.* **297**, 211–225.

Ma L., Chabaux F., Pelt E., Granet M., Sak P. B., Gaillardet J., Lebedeva M. and Brantley S. L. (2012) The effect of curvature on weathering rind formation: evidence from Uranium-series isotopes in basaltic andesite weathering clasts in Guadeloupe. *Geochim. Cosmochim. Acta* **80**, 92–107.

Maher K. (2010) The dependence of chemical weathering rates on fluid residence time. *Earth Planet. Sci. Lett.* **294**, 101–110.

Maher K. and Chamberlain C. P. (2014) Hydrologic regulation of chemical weathering and the geological carbon cycle. *Science* **343**, 1502. https://doi.org/10.1126/science.1250770.

Maher K., DePaolo D. J. and Lin J. C. F. (2004) Rates of silicate dissolution in deep-sea sediment: In situ measurement using U-234/U-238 of pore fluids. *Geochim. Cosmochim. Acta* **68**, 4629–4648.

Matthews, K.A., Goldstein, S., Norman, D., Nunn, A., Murrell, M., 2008. Eos Trans. AGU, 89, Fall Meeting Suppl., V13A-2090.

McGregor H. V., Hellstrom J., Fink D., Hua Q. and Woodroffe C. D. (2011) Rapid U-series dating of young fossil corals by laser ablation MC-ICPMS. *Quatern. Geochronol.* **6**, 195–206.

Mertz-Kraus R., Jochum K. P., Sharp W. D., Stoll B., Weis U. and Andreae M. O. (2010) In situ 230$^{\mathrm{Th}}$-232Th-234U-238U analysis of silicate glasses and carbonates using laser ablation single-collector sector-field IPC-MS. *J. Analyt. At. Spectromet.* **25**, 1895–1904.

Navarre-Sitchler A., Steefel C., Sak P. and Brantley S. L. (2011) A predictive model for weathering rind formation on basalt. *Geochim. Cosmochim. Acta* **75**, 7644–7667.

Pavich M. (1986) Process and rates of saprolite production and erosion on a foliated granitic rock of the Virginia Piedmont. In *Rates of Chemical Weathering of Rocks and Minerals* (eds. S. Colman and D. Dethier). Academic Press, London.

Pelt E., Chabaux F., Innocent C., Navarre-Sitchler A. K., Sak P. B. and Brantley S. L. (2008) Uranium-thorium chronometry of weathering rinds: rock alteration rate and paleo-isotopic record of weathering fluids. *Earth Planet. Sci. Lett.* **276**, 98–105.

Plater A. J., Ivanovich M. and Dugdale R. E. (1992) Uranium series disequilibrium in river sediments and waters: the significance of anomalous activity ratios. *Appl. Geochem.* **7**, 101–110.

Potter E.-K., Stirling C. H., Wiechert U. H., Halliday A. N. and Spotl C. (2005) Uranium-series dating of corals in situ using laser-ablation MC-ICPMS. *Int. J. Mass Spectromet.* **240**, 27–35.

Rosholt J., Doe B. and Tatsumoto M. (1966) Evolution of the isotopic composition of uranium and thorium in soil profiles. *Geol. Soc. Am. Bull.* **77**, 987–1004.

Sak P. B., Fisher D. M., Gardner T. W., Murphy K. and Brantley S. L. (2004) Rates of weathering rind formation on Costa Rican basalt. *Geochim. Cosmochim. Acta* **68**, 1453–1472.

Sak P. B., Murphy M., Ma L., Gaillardet J., Herdon E. M., Daniel C. and Brantley S. L. (2018) From unweathered core to regolith: rates and trends of in situ chemical weathering on tropical volcanic island (Bass Terre Island, French Guadeloupe). *Chem. Geol.* **498**, 17–30.

Sak P. B., Navarre-Sitchler A. K., Miller C. E., Daniel C. C., Gailardet J., Buss H. L., Lebedeva M. I. and Brantley S. L. (2010) Controls on rind thickness on basaltic andesite clasts weathering in Guadeloupe. *Chem. Geol.* **276**, 129–143.

Samper A., Quidelleur X., Lahitte P. and Mollex D. (2007) Timing of effusive volcanism and collapse events within an oceanic arc island: Basse-Terre, Guadeloupe archipelago (Lesser Antilles Arc). *Earth Planet. Sci. Lett.* **258**, 175–191.

Sarin M. M., Krishnaswami S., Somayajulu B. L. K. and Moore W. S. (1990) Chemistry of uranium, thorium, and radium isotopes in the Ganga-Brahmaputra river system – weathering processes and fluxes to the Bay of Bengal. *Geochim. Cosmochim. Acta* **54**, 1387–1396.

Shirvington P. J. (1983) Fixation of radionuclides in the 238U decay series in the vicinity of mineralized zones: 1. The Austatom Uranium Prospect, Northern Territory, Australia. *Geochim. Cosmochim. Acta* **47**, 403–412.

Spooner P. T., Chen T., Robinson L. F. and Coath C. D. (2016) Rapid uranium-series age screening of carbonates by laser ablation mass spectrometry. *Quatern. Geochronology* **31**, 28–39.

Stirling C. H., Lee D. C., Christensen J. N. and Halliday A. N. (2000). *Geochim. Cosmochim. Acta* **64**, 3737–3750.

Suresh P. O., Dosseto A., Hesse P. P. and Handley H. K. (2013) Soil formation rates determined from uranium-series isotope disequilibria in soil profiles from southeastern Australian Highlands. *Earth Planet. Sci. Lett.* **379**, 26–37.

Sylvester Pau and Jackson Simo (2016) A brief history of laser ablation inductively coupled plasma mass spectrometry (LA–ICP–MS). *Elements* **12**, 307–310. https://doi.org/10.2113/gselements.12.5.307.

Valle N., Verney-Carron A., Sterpenich J., Libourel G., Deloule E. and Jollivet P. (2010) Elemental and isotopic (29Si and 18O) tracing of glass alteration mechanisms. *Geochim. Cosmochim. Acta* **74**, 3412–3431.

Verney-Carron A., Gin S. and Libourel G. (2008) A fractured roman glass block altered for years in seawater: analogy with nuclear glass in a deep geological repository. *Geochim Cosmochim. Acta* **72**, 5372–5385.

Vigier N., Bourdon B., Turner S. and Allegre C. J. (2001) Erosion timescales derived from U-decay series measurements in rivers. *Earth Planet. Sci. Lett.* **193**, 485–499.

Walker J., Hays P. and Kasting J. (1981) A negative feedback mechanism for the long-term stabilization of Earth's surface temperature. *J. Geophys. Res.* **86**, 9776–9782.

Associate editor: Claudine Stirling